

## Explosive erosion during the Phoenix landing exposes subsurface water on Mars

Manish Mehta<sup>a,\*</sup>, Nilton O. Renno<sup>a,b</sup>, John Marshall<sup>c</sup>, M. Rob Grover<sup>d</sup>, Anita Sengupta<sup>d</sup>, Neal A. Rusche<sup>a</sup>, Jasper F. Kok<sup>a,b,i</sup>, Raymond E. Arvidson<sup>e</sup>, Wojciech J. Markiewicz<sup>f</sup>, Mark T. Lemmon<sup>g</sup>, Peter H. Smith<sup>h</sup>

<sup>a</sup> Dept. of Atmospheric, Oceanic and Space Sciences, University of Michigan, 2455 Hayward St., Ann Arbor, MI 48109, USA

<sup>b</sup> Applied Physics Program, University of Michigan, Ann Arbor, MI 48109, USA

<sup>c</sup> Carl Sagan Center, SETI Institute, Mountain View, CA 94043, USA

<sup>d</sup> NASA Jet Propulsion Laboratory, Section 313, Pasadena, CA 91109, USA

<sup>e</sup> Dept. of Earth and Planetary Sciences, Washington University in St. Louis, St. Louis, MO 63130, USA

<sup>f</sup> Max Planck Institute for Solar System Research, Max-Planck-Str. 2, Katlenburg-Lindau 37191, Germany

<sup>g</sup> Dept. of Atmospheric Sciences, Texas A&M University, College Station, TX 77843, USA

<sup>h</sup> Dept. of Planetary Sciences, University of Arizona, Tucson, AZ 85721, USA

<sup>i</sup> Advanced Studies Program, National Center for Atmospheric Research Boulder, CO 80305, USA

### ARTICLE INFO

#### Article history:

Received 11 August 2009

Revised 6 October 2010

Accepted 10 October 2010

Available online 16 October 2010

#### Keywords:

Ices

Cratering

### ABSTRACT

While steady thruster jets caused only modest surface erosion during previous spacecraft landings on the Moon and Mars, the pulsed jets from the Phoenix spacecraft led to extensive alteration of its landing site on the martian arctic, exposed a large fraction of the subsurface water ice under the lander, and led to the discovery of evidence for liquid saline water on Mars. Here we report the discovery of the 'explosive erosion' process that led to this extensive erosion. We show that the impingement of supersonic pulsed jets fluidizes porous soils and forms cyclic shock waves which propagate through the soil and produce erosion rates more than an order of magnitude larger than that of other jet-induced processes. The understanding of 'explosive erosion' allows the calculation of bulk physical properties of the soils altered by it, provides insight into a new behavior of granular flow at extreme conditions and explains the rapid alteration of the Phoenix landing site's ground morphology at the northern arctic plains of Mars.

© 2010 Elsevier Inc. All rights reserved.

### 1. Introduction

On May 25th 2008, the Phoenix spacecraft landed on the martian arctic to study the local environment and its potential for sustaining life (Smith et al., 2009). The search for water has been an important goal of the mission because liquid water is an essential ingredient for life as we know it (e.g., Renno et al., 2009). Here, we report the discovery of the erosion process that rapidly removed 5–18 cm thick layers of soil (Smith et al., 2009; Sizemore et al., 2009), first exposing water ice at the landing site (Renno et al., 2009), and leading to the discovery of evidence for liquid saline water on Mars (Renno et al., 2009). The understanding of this process allowed the calculation of bulk physical properties of the soil at the Phoenix landing site. This study also provides information on site contamination that may have occurred during the landing phase. Along with new developments in granular flow, the discovery of the 'explosive erosion' process reported here has important implications for engineering and science.

Brief interactions of the jets from three non-pulsed engines of the Viking landers (with 2230 Newtons of thrust) with the martian soil caused only modest surface erosion during landing (Shorthill

et al., 1976a,b). However, Phoenix's 12 engines (with 30% less total thrust) pulsating at 10 Hz with an average impingement pressure of only 1/10 of the Earth's sea level pressure (Renno et al., 2009), caused extensive erosion of the landing site, and exposed the subsurface ice under the lander over a radius between 75 and 85 cm from its centerline (Appendix A) (Smith et al., 2009). The Phoenix inertial measurement unit indicates that lift loss started when the spacecraft was 5 m above the surface, while descending at ~2.6 m/s, followed by ground effects and a reduction in the spacecraft descent velocity (Figs. S1–S3, Supplementary material) (Desai et al., 2008). This suggests that the jets interacted with the soil for less than 2 s. Although unlikely, minor incipient erosion may have occurred while the spacecraft was above 5 m (Clark, 1970). To provide more contexts to our investigation, the aerodynamic loads and rates during the Phoenix spacecraft entry, descent and landing sequence is presented in Section 1 of the Supplementary material.

It has been known that jet impingement produces soil erosion and craters through four distinct physical processes: (i) the dragging of surface soil particles by viscous shear erosion (VSE) when the forces caused by the jet's shear stress exceed the cohesive and frictional forces between particles, as occurred during previous landings on Mars and the Moon (Shorthill et al., 1976a,b; Christensen et al., 1967). The formation of transient craters with steep walls occurs by a combination of two distinct processes

\* Corresponding author.

E-mail address: [manishm@umich.edu](mailto:manishm@umich.edu) (M. Mehta).

termed (ii) bearing capacity failure (BCF) and (iii) diffusion-driven flow (DDF) when the jet’s ground pressure exceeds the shear strength of the soil (Metzger et al., 2009a,b). (iv) The removal of soil when gases from the thruster jets rapidly escape from the granular pore space causing diffuse gas erosion (DGE), a single eruption event when the engines shut-down (Metzger et al., 2009a,b; Scott and Ko, 1968). Here, we report the discovery of a fifth process (v), which we name diffusive gas explosive erosion (DGEE) or ‘explosive erosion’ that dominates the erosion process when supersonic pulsed jets impinge into soils which generate high pore pressure gradient forces to soil weight ratios,  $\Delta P^*$ .

**2. Experimental methods**

Here, scaling analysis of laboratory experiments and numerical simulations are used to study the erosion caused by the Phoenix landing on Mars. Scaling of the thruster jet–soil system indicates that the erosion dynamics due to retro-propulsion-derived spacecraft landings on Mars can be simulated by laboratory experiments on Earth. Hence, the terms “experiments” and “laboratory simulations” are used interchangeably in the paper. Similarity can be achieved by matching the nondimensional numbers that scale gravitational ( $F_g$ ), interparticle ( $F_\sigma$ ), pore pressure gradient ( $F_p$ ) and aerodynamic ( $F_{aero}$ ) forces on the granular media (Fig. 1) (Balme and Hagermann, 2006; Neakrase and Greeley, 2009; Greeley and Iversen, 1985) or by simulating these forces in the absolute scale.  $F_{aero}$  on the particle is dependent on the jet’s shear stress and it has two components: the lift force which is perpendicular to the jet and drag force which is parallel to the flow. The interparticle forces which are a function of the particle size include cohesion, van der Waals, electrostatics and moisture (Neakrase and Greeley, 2009). The Magnus lifting force due to particle rotation and Saffman force due to shearing flow is less than a percent of the particle weight (Kok and Renno, 2010) and has been neglected in our scaling laws. It is also important to ensure that the jet impingement dynamics for the experiments such as the pulse width, frequency and jet orientation are accurately simulated to the performance of the Phoenix descent engines as shown in Table 1.

We studied 0.75–3.00 s long interactions of dry N<sub>2</sub> jets from a pair of subscale Phoenix engine nozzles with a granular bed of

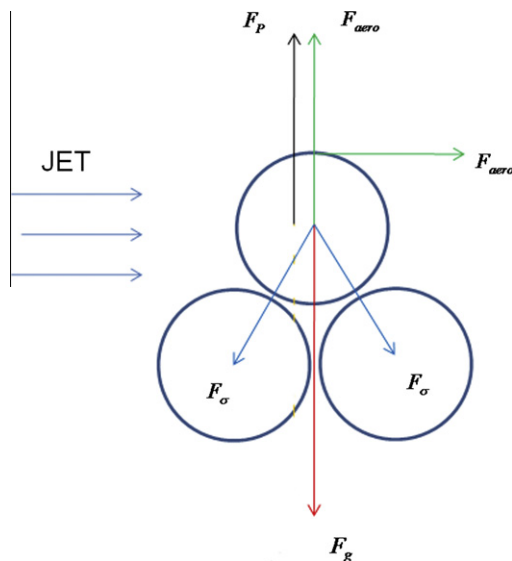


**Fig. 1.** Sketch of the main forces acting on soil particles during jet-induced erosion. Although depicted that the exhaust plume is incoming from left to right, it can be in any direction during the erosion process.

**Table 1**

Thruster parameters of a pair of Phoenix rocket motors and experimental cold flow thrusters.

Parameters	Variable	Units <sup>c</sup>	Full scale <sup>a</sup>	½ scale <sup>b</sup>
Jet total pressure at inlet (kPa)	–	M/LT <sup>2</sup>	1240	1240
Jet total temperature at inlet (K)	–	Θ	1116	300
Jet pulse frequency (Hz)	–	1/T	10	10
Jet pulse width (s)	$T_{PW}$	T	~0.055	~0.065
Jet firing duration (s)	$t_L$	T	<2.0	≤3.0
Nozzle diameter at exit (cm)	$D$	L	6.25	3.13
NH <sub>3</sub> exhaust mass fraction (a.u.)	$f_{NH_3}$	–	0.49	0.0
Maximum thrust (N)	–	ML/T <sup>2</sup>	~600	~160

<sup>a</sup> Phoenix MR-107N rocket motor parameters during constant velocity terminal descent.

<sup>b</sup> Experimental N<sub>2</sub> cold flow thruster parameters.

<sup>c</sup> M = mass; L = length; T = time; Θ = temperature.

martian simulant of various particle size distributions in a pressure-controlled chamber. Brief plume–soil interactions of steady and 10 Hz pulsed jets at ~300 K with a ~65 ms pulse width (Fig. 2) at various static altitudes are studied in a ~4000 m<sup>3</sup> chamber at NASA Ames Research Center’s Planetary Aeolian Laboratory (PAL). The vacuum chamber was set to atmospheric pressures between martian and terrestrial near-surface ambient conditions. All jets impinge normally with respect to the soil bed. The contours of the pair of Phoenix descent rocket engine motor (REM) nozzles and the spacecraft configuration including the lander deck are all ½ scale models as depicted along the +z and –x directions in Fig. 3A and B. All dimensional parameters and their corresponding notations and units, used to define the multiphase flow, are tabulated in Table 2.

Pressure transducers installed in the nozzle inlets were used to monitor the stagnation pressure in the thruster simulator and assure that its magnitude and temporal profile were similar to that in the combustion chamber of the Phoenix descent engines during the landing phase. The nozzle pressure ratio (NPR), ratio of the stagnation pressure to ambient pressure, was nearly identical between subscale and full-scale systems. The thruster inlet stagnation pressure vs. time graph known as a thrust cycle for a 10 Hz pulsed jet is shown in Fig. 2 (Plemmons et al., 2008). There are four regimes for each cycle which spans 0.1 s: thrust rise, ‘steady’

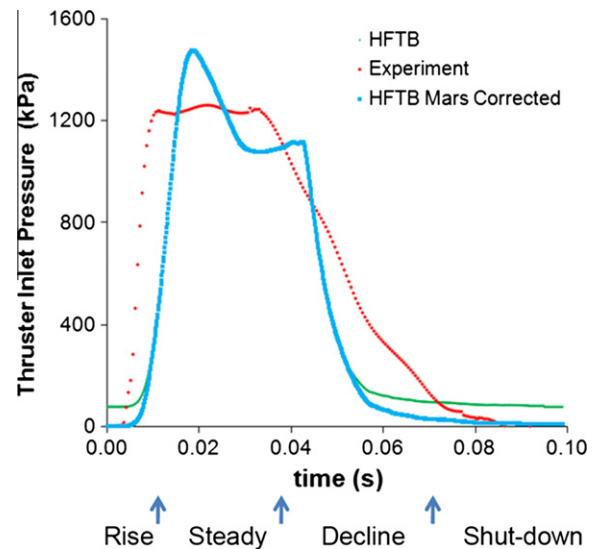


**Fig. 2.** ½ scale Phoenix cold gas thrusters pulsating at 10 Hz with a ~65 ms pulse width are used in the laboratory simulations (experiment). Data from a single thrust cycle of the laboratory simulation at Mars atmospheric pressure is compared with that from the Phoenix REM thrusters hot fire testbed (HFTB) performed at Earth atmospheric pressure and corrected for Mars atmosphere conditions.

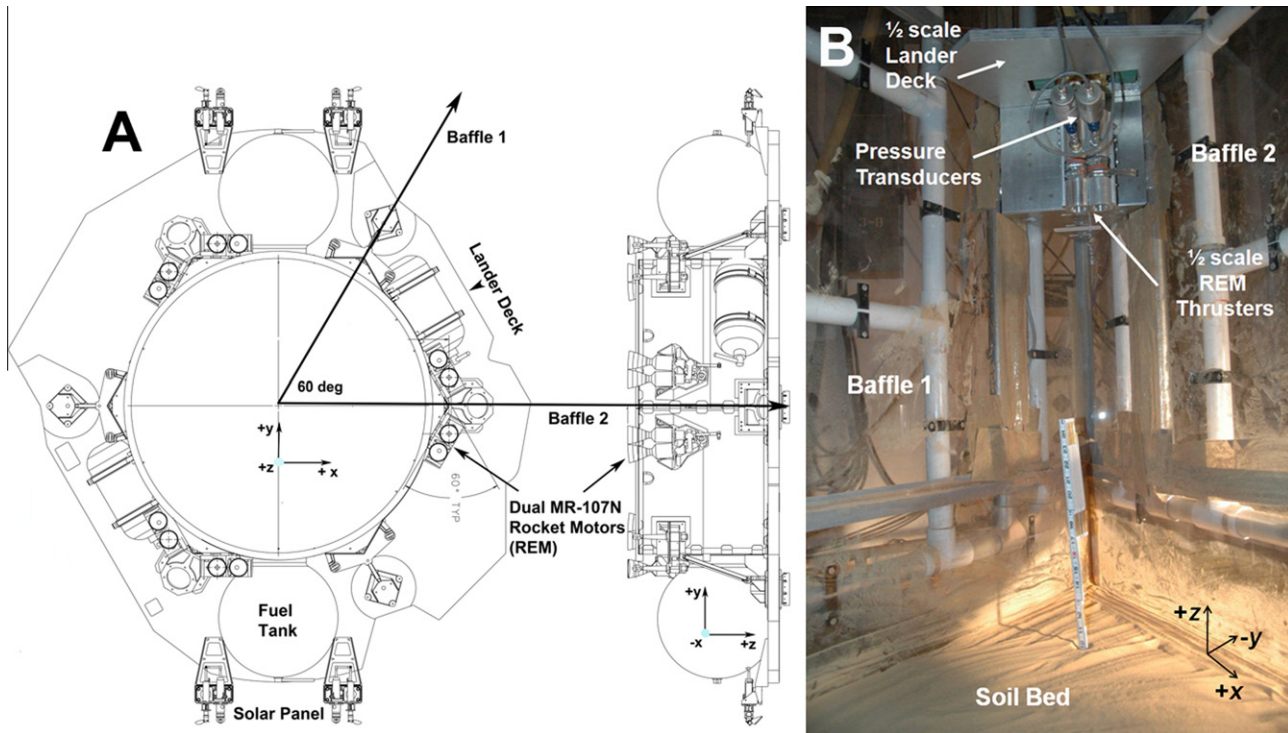


**Fig. 3.** (A) Top-down schematic along the  $+z$  axis and side (along the  $-x$ -axis) views of the Phoenix spacecraft which shows the placement of the transparent baffles 1 and 2 and thrusters. (B) An isometric photograph of the laboratory simulations at PAL.

**Table 2**  
Dimensional parameters at pre-jet impact conditions based on scaling relations.

Parameters	Variable	Units <sup>d</sup>	Reference	Full scale <sup>a</sup>	1/2 scale <sup>c</sup>
Friction velocity (m/s)	$u_*$	L/T	Shao and Lu (2000)	~88.9	~35.6
Threshold friction velocity (m/s)	$u_{*t}$	L/T	Shao and Lu (2000)	1.3	0.5
$A_N$ (a.u.)	$A_N$	–	Shao and Lu (2000)	0.0123	0.0123
$K$ ( $m^4/kg s^2$ )	$\kappa$	$L^4/MT^2$	Shao and Lu (2000)	$3 \times 10^{-4}$	$3 \times 10^{-4}$
Gas diffusion time (s) <sup>b</sup>	$\tau$	T		~33–1	~20–1
Jet impingement pulse period (s)	$t_{imp}$	T		0.1	0.1
Soil depth (cm)	$l$	L		5–18	5–20
Porosity (%) <sup>b</sup>	$n$	–		~50	50
Gas viscosity at exit ( $kg/m s$ )	$\mu$	M/LT		$9.4 \times 10^{-6}$	$3.5 \times 10^{-6}$
Permeability ( $m^2$ ) <sup>b</sup>	$k$	$L^2$		$7.1-0.2 \times 10^{-11}$	$7.1-0.2 \times 10^{-11}$
Cohesion (kPa)	$c$	M/LT <sup>2</sup>		0.3–1.9	1.3
Angle of internal friction (°)	$\theta_i$	–		~30	33
Soil particle density ( $kg/m^3$ )	$\rho_p$	M/L <sup>3</sup>		3000–2650	1300
Soil shear strength (kPa) <sup>b</sup>	$Y$	M/LT <sup>2</sup>	Terzaghi (1943)	Varies	Varies
Particle size ( $\mu m$ )	$d$	L		~160	~160
Impingement pressure (kPa) <sup>b</sup>	$P_{imp}$	M/LT <sup>2</sup>		~15	~15
Gravitational acceleration ( $m/s^2$ )	$g$	L/T <sup>2</sup>		3.71	9.8
Pore pressure (kPa) <sup>b</sup>	$P_p$	M/LT <sup>2</sup>	Balme and Hagermann (2006)	Varies	Varies
Granular speed of sound ( $m/s$ ) <sup>b</sup>	$c_s$	L/T		Varies	Varies
Atmospheric pressure (Pa)	$P_{amb}$	M/LT <sup>2</sup>		~858	~832
Atmospheric temperature (K)	$T_{amb}$	$\Theta$		~243	~280
Jet pressure at exit (kPa)	$P_e$	M/LT <sup>2</sup>		3.24	3.09
Jet density at exit ( $kg/m^3$ )	$\rho_a$	M/L <sup>3</sup>		0.03	0.19
Jet velocity at exit (m/s)	$U_e$	L/T		1929	712
Jet mass flow rate ( $kg/s$ )	$\dot{m}$	M/T		0.32	0.22

<sup>a</sup> Data obtained from fine basaltic sand at Viking 2 Landing Site on Mars (Shaw et al., 2009) and Phoenix rocket motor parameters.

<sup>b</sup> Properties significantly change from pre-jet impact conditions during DGEE.

<sup>c</sup> Data obtained for simulant-type S and cold flow thruster parameters.

<sup>d</sup> M = mass; L = length; T = time;  $\Theta$  = temperature.

thrust, thrust decline and thrust shut-down For all tests, the maximum thruster chamber pressure and temperature are 1.2 MPa and 300 K, respectively (Table 1).

Transparent plexiglass baffles (baffles 1 and 2) were used to simulate the planes of symmetry between neighboring pairs of

thruster jets as shown in Fig. 3A (Romine et al., 1973; Huseman and Bomba, 2000) and to visualize the erosion process through still and hi-speed imaging (Schultz et al., 2007; Metzger et al., 2009a,b). When multiple jets impinge on the surface, flow stagnation planes develop between groups of thrusters (Huseman and Bomba, 2000;

Romine et al., 1973). The trajectories of fine soil particles loosely follow these planes. Therefore, a 60° test section was developed to simulate the fluid dynamic effects of the outboard REM thrusters.

The quarter-space technique (Schultz et al., 2007) described below is used in all PAL experiments to approximately visualize the axisymmetric crater growth process. All high speed images are taken along the  $x$ - $z$  plane (baffle 2) in the direction of the  $+y$ -axis which is directed into the page and the origin is at the apex of the wedge as depicted in Fig. 4A and B. These images at full resolution of  $1280 \times 1024$  pixels are taken normal to baffle 2 at a frame rate of 500 images per second and shutter speed of 1 ms. The high-speed camera is located 30 cm from the baffle plane (Fig. 4C) and focused on the impingement region's  $x$ - $y$ - $z$  coordinates of: (30 cm, 0 cm, 20 or 5 cm). The test section which shows a 2-D layer of granular media is illuminated with 750 W lamps on either side of the camera. The high-speed camera operates with a wide angle lens which allows a coverage width of 75 cm. Based on test setup configuration, the impingement centerline point on the granular media is at an  $x$ - $y$ - $z$  coordinate of: (30.0 cm, 5.6 cm, 20.0 or 5.0 cm). In cylindrical coordinates, the  $r$ - $\theta$ - $z$  values are: (30 cm, 10.6°, 20 or 5.0 cm). All data extrapolated from high speed images are taken along the  $x$ - $z$  plane at  $\theta = 0^\circ$  (baffle 2). Post site alteration data is taken from still images

along the  $x$ - $z$  plane at  $\theta = 0^\circ$  and  $\theta = 60^\circ$  (baffle 1) and isometric images and measurements.

In order to account for the effects of lower martian gravity, low-density crushed walnut shells were used to simulate the weight,  $F_g$ , of soil particles on Mars (Greeley et al., 1980). These martian simulants partitioned into four different particle size distributions, were used in the experiments: (i) poorly sorted fine sand (S) (diameter,  $d \sim 160 \mu\text{m}$ ), (ii) fine silt/dust (F) ( $d < 15 \mu\text{m}$ ), (iii) large coarse sand (C) ( $d = 850\text{--}2500 \mu\text{m}$ ), and (iv) bimodal mixture of fine silt/dust with fine sand (B) (Table 3). The simulants were sieved to resemble the various size distributions of basaltic sand found on Mars (Shaw et al., 2009) to accurately simulate interparticle forces. The simulant properties were determined by direct shear, constant/variable head permeability and relative density tests performed in controlled laboratory conditions at 300 K and 5–20% relative humidity which was representative of the conditions of the NASA Ames vacuum chamber facility.

## 2.1. Scaling analysis

Erosion rates and dynamics depend on the forces acting on the granular media (Fig. 1) and modes (Fig. 2) of the impinging jets. It follows from nondimensional analysis that the forces caused by

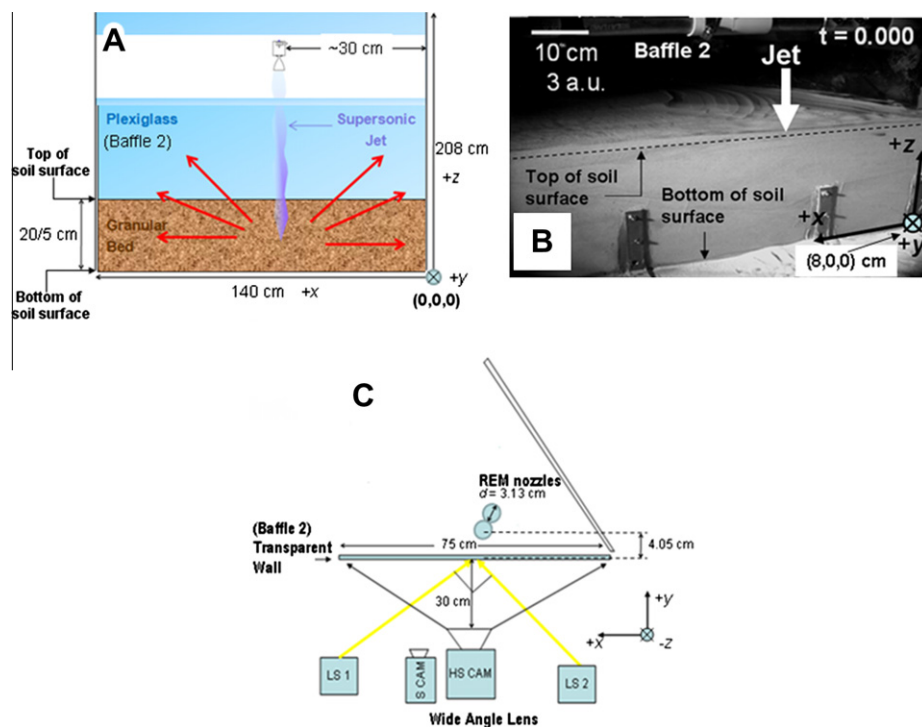


**Fig. 4.** (A) A schematic of the impingement of supersonic pulsed jets on porous soils. The quarter-space technique (Schultz et al., 2007) with the high-speed camera viewing along the positive  $y$ -axis and focusing on the plexiglass symmetry-plane ( $x$ - $z$  plane) is used to analyze the jet–soil interaction. (B) An annotated monochromatic image of the test section along the  $x$ - $z$  plane at pre-jet impact conditions ( $t = 0.0$  s). (C) A schematic of the experimental setup looking along the  $-z$  axis. Shows the positioning of the test section, high speed (HS CAM) and still (S CAM) cameras and focused lights sources (LS) depicted by yellow arrows. The black arrows originating from the HS CAM depict the coverage area. (For interpretation of the references to color in this figure legend, the reader is referred to the web version of this article.)

**Table 3**

Measurements of the physical properties of the martian soil simulant (crushed walnut shells) used in the laboratory simulations.

Soil simulant	Particle diameter ( $\mu\text{m}$ )	Mean diameter ( $\mu\text{m}$ ) <sup>a</sup>	Cohesive strength (kPa)	Permeability coefficient (cm/s)	Porosity (a.u.)	Angle of friction ( $^\circ$ )	Crater volume ratio (a.u.)
Fine silt/fine sand (B)	2–200	~BI	5.0 ( $\pm 1.5$ )	0.0003 ( $\pm 2e-5$ )	0.45 ( $\pm 0.05$ )	31 ( $\pm 2.0$ )	0.16
Fine sand (S)	2–200	~160	1.3 ( $\pm 0.3$ )	0.0021 ( $\pm 0.001$ )	0.50 ( $\pm 0.05$ )	33 ( $\pm 2.5$ )	0.20
Coarse grain (C)	850–2500	~1500	0.0 ( $\pm 0.25$ )	0.3000 ( $\pm 0.1$ )	0.30 ( $\pm 0.03$ )	35 ( $\pm 2.0$ )	0.01
Fine silt (F)	2–25	<15	7.5 ( $\pm 1.0$ )	0.0002 ( $\pm 3e-5$ )	0.73 ( $\pm 0.10$ )	28 ( $\pm 2.0$ )	0.65

<sup>a</sup> BI – 50% fine silt and 50% fine sand by volume.

the impinging jets on the soil are scaled by matching the ratio of the kinetic with the internal energy (hypersonic similarity parameter,  $KE/IE$ ) of the plume (Eq. (1)) (Plemmons et al., 2008), the jet expansion ratio ( $e$ , Eq. (2)) (Plemmons et al., 2008), and the plume's nozzle exit Mach number ( $M_e$ , Eq. (1)), specific heat ratio ( $\gamma$ , Eq. (1)) and Reynolds number ( $Re_g$ , Eq. (3)). Along with matching the jet dynamics, the erosion dynamics are scaled (Appendix B) by matching the densimetric Froude number ( $Fr_d$ , Eq. (4)) (Mazurek and Rajaratnam, 2005; Greeley and Iversen, 1985), the soil strength scaling parameter ( $\beta$ , Eq. (5)) (Holsapple, 1993), the nondimensional threshold friction velocity ( $u_{*t}/u_*$ , Eq. (6)) (Greeley and Iversen, 1985), the ratio of the characteristic diffusion time in the vertical component with jet pulse period ( $\tau/t_{imp}$ , Eq. (7)) and the normalized pressure gradient within the soil ( $\Delta P^*$ , Eq. (8)) (Balme and Hagermann, 2006). From dimensional analysis (Appendix B), the important dimensional terms are shown in Table 2 and the scaling laws are tabulated in Table 4 and defined as follows:

$$\frac{KE}{IE} = \gamma(\gamma - 1)M_e^2 \quad (1)$$

$$e = \frac{P_e}{P_{amb}} \quad (2)$$

$$Re_g = \frac{\rho_a D U_e}{\mu} \quad (3)$$

$$Fr_d = \frac{U_e}{\sqrt{\frac{\rho_p}{\rho_a} g d}} \quad (4)$$

$$\beta = \frac{Y}{\rho_a U_e^2} \quad (5)$$

$$\frac{u_{*t}}{u_*} = \sqrt{\frac{A_N \left( \frac{\rho_p}{\rho_a} g d + \frac{\kappa}{\rho_a d} \right)}{u_*^2}} \quad (6)$$

$$\frac{\tau}{t_{imp}} = \left( \frac{2l^2 n \mu}{k P_{imp}} \right) \frac{1}{t_{imp}} \quad (7)$$

$$\Delta P^* = \frac{3(P_p - P_{amb})}{2\rho_p g d} = \frac{3\Delta P}{2\rho_p g d} \quad (8)$$

**Table 4**  
Normalized parameters at pre-jet impact conditions based on scaling relations.

Normalized parameters	Variable	Full scale <sup>a</sup>	½ scale <sup>c</sup>
Expansion ratio	$e$	3.8	3.7
Exit Mach number	$M_e$	4.7	4.8
Nondimensional threshold friction velocity	$u_{*t}/u_*$	~0.015	0.014
Nozzle pressure ratio	$NPR$	~1500	1550
Densimetric Froude number	$Fr_d$	250	230
Gas Reynolds number	$Re_g$	$3.4 \times 10^5$	$12.7 \times 10^5$
Particle $Re$ number <sup>b</sup>	$Re_p$	$0.7 \times 10^3$	$2 \times 10^3$
Strength scaling parameter	$\beta$	~0.4	~0.3
$KE/IE$ plume	–	11.4	12.7
Diffusion time scale <sup>b</sup>	$\tau/t_{imp}$	~330–10	200–6
Specific heat ratio	$\gamma$	~1.38	1.40
Nozzle area ratio	–	20.7	20.7
Knudsen number	$Kn$	0.03	0.05
Altitude	$h/D$	8–80	8–60
Normalized pressure gradient <sup>b</sup>	$\Delta P^*$	>2500	>1800

<sup>a</sup> Data taken from fine basaltic sand at Viking 2 Landing Site on Mars (Shaw et al., 2009) and Phoenix rocket motor parameters.

<sup>b</sup> Properties significantly change from pre-jet impact conditions during DGEE.

<sup>c</sup> Data obtained from simulant-type S and cold flow thruster parameters.

The constants,  $A_N (= \sqrt{f(Re_{*t})})$  and  $\kappa$ , are proportional to interparticle forces (Shao and Lu, 2000). The soil strength,  $Y$ , is dependent on cohesive strength ( $c$ ), effective normal stress and angle of internal friction ( $\theta_i$ ) (Terzaghi, 1943).  $A_N$  is weakly dependent on  $Re_{*t}$  for particle sizes between 30  $\mu\text{m}$  and 1300  $\mu\text{m}$ .

We briefly discuss our assumptions and add further detail in the usage of these scaling laws. From normalizing the compressible Navier–Stokes equations and the boundary conditions of the exhaust plume (Schlichting and Gersten, 2000), the five most important nondimensional terms in simulating these exhaust flows are the exit Mach number, NPR, specific heat ratio, jet expansion ratio and the gas Reynolds number. The  $M_e$ , NPR,  $e$  and  $\gamma$  are matched for our flows as observed in Table 4. For the  $N_2$  jets and rocket plume which are in the turbulent regime (Table 4), the gas Reynolds number ( $Re_g$ ) has a small effect on aerodynamic forces due to the Reynolds Number Similarity (Townsend, 1956). The aerodynamic forces are dependent on the lift and drag coefficients, the dynamic pressure and the particles cross sectional area. These aerodynamic coefficients are relatively constant and independent of  $Re_g$  within the turbulent regime.

The nondimensional terms for simulating jet–soil interactions are derived by Buckingham's Pi theory (Buckingham, 1914) as shown in Appendix B and further confirmed by normalizing the soil transport equations (Greeley and Iversen, 1985). The bulk particle Reynolds number ( $Re_p$ ) for packed granular beds which is dependent on particle size and porosity (Appendix B, Eq. (B7)), for both full-scale and subscale simulations indicate that the flow is near or within the turbulent regime (Table 4). According to the Burke–Plummer equation for  $Re_p \geq 1000$  (Bird, 1996), the friction factor ( $C_d$ ) is relatively constant and independent of  $Re_p$  for average particle sizes tested and adequately simulates the viscous forces. Independently, neither the  $Fr$  nor the density ratio (Eq. (B5)) accurately describe sediment transport due to jet interactions, but the combination of the two parameters (Eq. (4)) show good correlation with erosion rates and crater profiles as proven by previous researchers (Greeley and Iversen, 1985; Mazurek and Rajaratnam, 2005; Neakrase and Greeley, 2009). The  $\beta$  parameter is not important for low cohesive and low bulk weight soils as observed on Mars and in our experiments. The nondimensional threshold friction velocity ( $u_{*t}/u_*$ ) is an important parameter because it determines whether the jet's viscous shear stress is capable of eroding soil grains when  $u_{*t}/u_* < 1$ . The numerator of Eq. (6) determines the required friction velocity to lift spherical particles by taking the summation of the aerodynamic, interparticle and gravitational forces and moments on a grain (Shao and Lu, 2000). The denominator of Eq. (6) is the friction velocity of the exhaust plume along the granular media which is calculated from Eq. (C3) (Appendix C) at a normalized radius of  $\sim 4$  from the plume centerline. Here, the velocity and density profiles were similar to the nozzle exit conditions and were obtained from computational fluid dynamic simulations of both full-scale and subscale jets. Since the particle size distribution is approximately equal between the simulant and martian soil (Goetz et al., 2009), we use the same aerodynamic roughness length,  $z_0$  (Appendix C, Eq. (C3)) when calculating the friction velocity (Eq. (6)) (Greeley et al., 2000). Eq. (7) is the ratio of time needed for diffusion of the exhaust plume to reach steady state to a soil depth of  $l$  (diffusion time) with respect to the jet's pulse period,  $t_{imp}$ . The  $\frac{D}{d}$  scale is orders of magnitude larger than unity which proves that microscopic effects due to gas diffusion on individual grains can be neglected (Mazurek and Rajaratnam, 2005) and the dynamics are governed by bulk properties.

The scaling analysis of cratering described above demonstrates similarity in the absolute forces and force ratios on the granular system between the laboratory simulations and the full-scale process of spacecraft landings on Mars (Table 4). Hence, this satisfies our main goal of simulating the dynamics of the exhaust plume

and soil particles during cratering. As a result, similar transient pressure distributions on the surface (Plemmons et al., 2008; Mehta et al., 2008; Van Norman and Novak, 2009), similar shock structure profiles of the exhaust plume (Plemmons et al., 2008; Mehta et al., 2008; Van Norman and Novak, 2009), and similar shear strength soil properties and soil weight occur between the laboratory experiments and full-scale system on Mars. In Section 6, we show that the normalized crater and deposition profiles and normalized erosion rates are similar in both our experimental results and observations at the Phoenix landing site. This similarity in the dynamic forces is critical for the quantitative simulation of the erosion and cratering dynamics caused during the Phoenix landing (Holsapple, 1993; Greeley et al., 1980). Certain scaling parameters can be neglected depending on which erosion process is dominant. For example, the normalized shear strength (Eq. (5)), pore pressure gradient (Eq. (8)) and diffusion time scale (Eq. (7)) parameters can be neglected for VSE dominant processes.

There are some limitations to these tests due to the fact that they were conducted at Earth's gravity and used exhaust jets composed of  $N_2$  at room temperature. Dynamic descent of thrusters during test firing was not pursued because of adding unknown complexity to the physics. However, static firing at various altitudes allowed us to integrate this function and obtain a representative mean value for erosion rates and crater dimensions. Due to the lighter weight of walnut shells, the soil simulant particles accelerate faster by a factor of  $\sim 2.2$  than soil particles on Mars, but the initial trajectories of the ejecta are adequately simulated because the inertial forces are similar in both at the near-field crater regime (near and within the crater). However, complete similarity of the kinematics is difficult to achieve. Within this regime, the drag ( $D$ ) and lift forces (Eq. (9)) are independent of the particle velocity,  $u_p$ , due to the valid assumption that the gas velocity,  $U_\infty$ , is much larger than the particle velocity. This is also supported by experimental observations. The density of the exhaust plume is denoted by  $\rho$  in Eq. (9).

$$D = \frac{1}{8} C_d \rho (U_\infty - u_p)^2 \pi \bar{d}^2 = \frac{1}{8} C_d \rho \pi \bar{d}^2 U_\infty^2 \left[ 1 - 2 \frac{u_p}{U_\infty} + \left( \frac{u_p}{U_\infty} \right)^2 \right] \\ \sim \frac{1}{8} C_d \rho \pi \bar{d}^2 U_\infty^2; \quad U_\infty \gg u_p \quad (9)$$

This is partly due to high particle collision frequencies which inhibit large increases in the particle acceleration relative to the exhaust plume. At far-field regimes, this assumption may not be valid for certain cases and further studies are needed to assess the lift and drag forces on the ejecta. Particle Reynolds number presents a large disparity between experiment and full-scale processes for clay-size particles ( $\sim 1 \mu\text{m}$ ) due to differences in exhaust plume viscosity. More importantly, we have not quantified here how each scaling parameter affects the erosion rates. Although these scaling laws described above prove to be theoretically valid, we conclude that this application needs to be confirmed by additional experimental and numerical simulations.

## 2.2. Determining average jet-induced erosion rates

The average erosion rates were calculated based on the radius and depth measurements of the final crater developed in each experiment. The error associated with these in situ measurements was less than 5%. The total crater volume ( $V_c$ ) was calculated assuming that it is a paraboloid with a volume:

$$V_c = \frac{1}{2} \pi r^2 h \quad (10)$$

where  $r$  is the radius of the crater and  $h$  is its depth. Knowing the duration of the jet impingement,  $t_L$ , the bulk density of the martian

simulant, and the crater volume, the average rate of mass ejected by the jets can be calculated. Some crater volumes (e.g., exposed surface) were geometrically calculated from a derivative of the paraboloid. This approach shows good agreement to the method of integrating infinitesimal parabolic contours. Physical dimensions and erosion rates are normalized by the pair of subscale thrusters' exit diameter (3.125 cm) and mass flow rate (0.22 kg/s), respectively, and therefore expressed as a dimensional units (a.u.). The normalized crater dimensions such as depth and exposed and crater radii are recorded in Table D.1, Appendix D. A mass correction term is used to estimate the erosion rate expected at the Phoenix landing site from the experimental data. This term is the density ratio between simulant and basaltic sand (factor of 2) and this mass scaling approach was confirmed by Greeley et al. (1982) using wind tunnel simulations to estimate the sediment flux due to dust devils on Mars.

## 3. Observations

There were four general experimental cases performed in this study: (i) pulsed and (ii) steady jets at Mars atmospheric pressure and (iii) pulsed and (iv) steady jets at Earth atmospheric pressure. The main goal of this study was to determine the effects of pulsed jets on granular media in tenuous atmospheres. These cases were selected to provide a range of data sets applicable to propulsion-derived spacecraft landings on planetary bodies. These 24 experiments tabulated in Table 5 would also provide a diverse range of erosion mechanisms observed by impinging jets.

Here, we will briefly discuss the various observations noted from the experiments conducted at the PAL facility. For all of the cases of pulsed jet impingement into simulant at martian atmospheric pressure, the soil was rapidly excavated to the hard surface and moved granular media outward in a radial fan reaching mean heights of  $\sim 3$  m ( $\sim 100$  a.u.) and radial distances of  $\sim 10$  m ( $\sim 300$  a.u.) as observed by real-time imaging. Highly dynamic granular structures within the soil bed were only observed with high-speed imaging. For example, bright radial granular fronts which originated below the thruster were seen propagating within the soil along the transparent baffle 2 plane, but not along baffle 1. Also, bubbling and semi-stratification of the soil below the thrusters were observed during each thrust shut-down phase. Upon complete excavation of the granular media before four thrust cycles (0.4 s), the ordered granular structures disappear and turbulent movement of soil is observed. These highly dynamic granular structures, the associated explosive energy and substantial rapid removal of soil were not seen for the impingement of pulsed and steady jets at Earth atmosphere or steady jets at Mars atmosphere.

For all cases at Earth atmosphere, the erosion was highly localized and resulted in the surficial removal of less than 5 cm of soil, leading to characteristic parabolic craters. The trajectories of the soil particles were mainly vertical with a maximum height of  $\sim 0.6$  m which did not extend outward beyond 0.5 m from the jet centerline. For pulsed jets during thrust shut-down phase, the crater slope would exceed the angle of internal friction leading to re-deposition of the crater.

For all cases of steady jets at Mars atmosphere, the soil was temporarily excavated to the hard surface within  $\sim 0.7$  s, forming a steep cylindrical crater which quickly re-deposited during the thrust shut-down phase. The soil trajectory was mainly vertical but a modest amount of simulant did extend outward to a radial distance from jet centerline and height of  $\sim 2$  m.

No signs of crater disturbances were noted due to the filling of the vacuum chamber to terrestrial atmospheres after each tests was completed. The suspension time of C-type, S-type, and F-type simulant within the martian atmosphere after test completion was

**Table 5**  
Test matrix.

Test	Jet height (m)	Soil depth (cm)	Soil simulant	Jet mode	Pulse frequency (Hz)	Test duration <sup>a</sup> (s)	$P_{amb}$ (kPa)	$P_{imp}$ (kPa)	$T_{amb}$ (K)	Dominant mechanism
1	0.26	20	B	Pulsed	10	1.50	0.800	18	287	DGEE
2	0.26	5	B	Pulsed	10	1.50	0.800	18	288	DGEE
3	0.26	5	B	Pulsed	10	3.00	0.864	18	288	DGEE
4	0.26	20	S	Pulsed	10	3.00	0.864	18	285	DGEE
5	0.41	20	S	Pulsed	10	3.00	0.864	22	288	DGEE
6	0.41	20	S	Pulsed	10	3.00	0.800	22	286	DGEE
7	0.74	20	S	Pulsed	10	3.00	0.864	11	285	DGEE
8	1.88	20	S	Pulsed	10	3.00	0.864	8	285	DGEE
9	0.26	20	S	Pulsed	10	1.50	0.800	18	287	DGEE
10	1.88	20	S	Pulsed	10	1.50	0.800	8	286	DGEE
11	0.26	5	S	Pulsed	10	1.50	0.800	18	287	DGEE
12	0.41	20	S	Pulsed	10	3.00	101.3	–	290	VSE
13	1.56	20	S	Pulsed	10	3.00	101.3	–	290	VSE
14	0.26	20	S	Pulsed	10	3.00	101.3	3	291	VSE
15	0.74	20	S	Pulsed	10	3.00	101.3	–	290	VSE
16	0.26	20	S	Steady	0	0.75	101.3	–	290	VSE
17	0.26	20	S	Pulsed	10	1.50	101.3	–	285	VSE
18	0.26	20	S	Steady	0	0.75	0.800	18	288	BCF/DDF
19	1.05	20	S	Steady	0	0.75	0.800	–	284	BCF/DDF
20	1.56	20	S	Steady	0	0.75	0.864	–	290	BCF/DDF
21	0.26	5	F	Pulsed	10	1.50	0.800	18	287	DGEE
22	0.26	20	F	Pulsed	10	1.50	0.800	18	288	DGEE
23	0.26	5	C	Pulsed	10	1.50	0.864	18	285	VSE
24	0.26	20	C	Pulsed	10	1.50	0.800	18	288	VSE

<sup>a</sup> Thrust duration  $\sim 0.5 \times$  test duration (for pulsed jets only).

less than 1 s, 300 s and 11,000 s, respectively. Distinct characteristic observations were noted for the four general cases by both high-speed and real-time imaging, and this led us to believe that different mechanisms and dynamics were involved as will be discussed in the following sections.

#### 4. Diffusive gas explosive erosion

##### 4.1. Results

To compare the various jet-induced erosion and crater growth processes observed in the experiments, we developed normalized erosion rate vs. normalized altitude profiles from the numerous test cases shown in Fig. 5. These comparisons are made with the thrust duration and thrust being equivalent for all cratering processes studied which is approximately similar to the Phoenix spacecraft descent time and thrust per unit area within the last 5 m prior to landing (Table 5). DGEE, resulting from pulsed jet impingement, occurs for thruster altitudes ranging from 0.26 to 2 m above the surface for all soil simulants tested, except coarse sand/granules (Tests 23 and 24). The average crater growth rate caused by DGEE, depicted by blue and red data points in Fig. 5 (Tests 1–11, 21, 22), is approximately five times greater than that caused by BCF/DDF, the dominant cratering mechanisms caused by steady (non-pulsed) jets at Mars atmospheric conditions illustrated by the green curve (Tests 18–20). Indeed, our laboratory experiments also show that DGEE at Mars atmospheric conditions removes 10–20 times more soil particles per unit thrust time than VSE either at Mars (Shorthill et al., 1976a,b; Romine et al., 1973), or at Earth's atmospheric conditions, where VSE dominates as illustrated by the yellow curve (Tests 12–15, 17). DGE was not observed in our tests.

The final crater morphology, calculated from isometric images (Fig. 6A), is shown in Figs. 6B, 7 and 8 as contour plots to depict the extent of erosion and cratering that occurred in each general test case. The colorbar denotes the normalized soil depth where negative and positive values correlate to depth of soil either eroded (shaded in blue) or deposited (shaded in red), respectively. Half-scale quarter section of the spacecraft is superimposed onto these

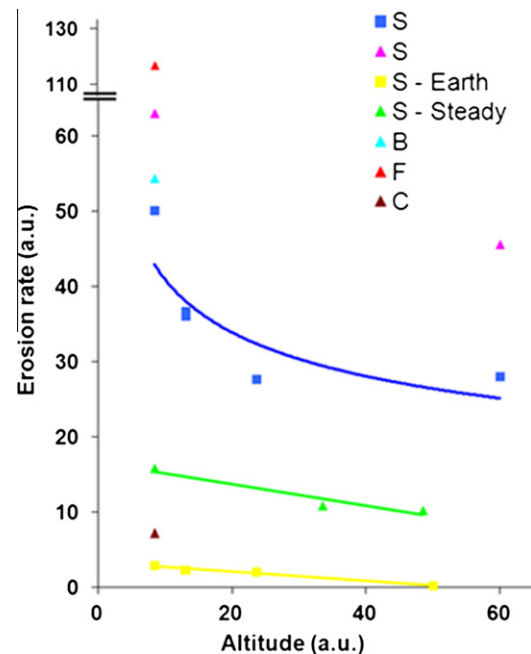


**Fig. 5.** Normalized erosion rate vs. normalized altitude for laboratory simulations with various soil simulants at Mars and Earth atmosphere conditions. The erosion rate is normalized by the jet's mass flow rate and the altitude is normalized by the nozzle exit diameter. All data points are for pulsed impinging jets at Mars atmosphere at 20 cm soil depth unless specified. Square and triangle box symbols denote 3 s and 1.5 s test durations, respectively; 0.75 s test duration for steady jets; The blue curve fitting line for the fine sand (S) experiments (Tests 4–8) is a power law polynomial, and the green (Tests 18–20) and yellow fitting lines (Tests 12–15) are linear. (For interpretation of the references to color in this figure legend, the reader is referred to the web version of this article.)

contour plots. Also included in these contour plots is the 90° sweep of the Robotic Arm which is depicted in a darker shade. All length scales ( $x$ ,  $y$  and  $z$ ) in these figures are normalized by the nozzle exit diameter,  $D$ . All values reported within this article and figures are obtained from the experiments (exp), and the full-scale ( $f_s$ ) length

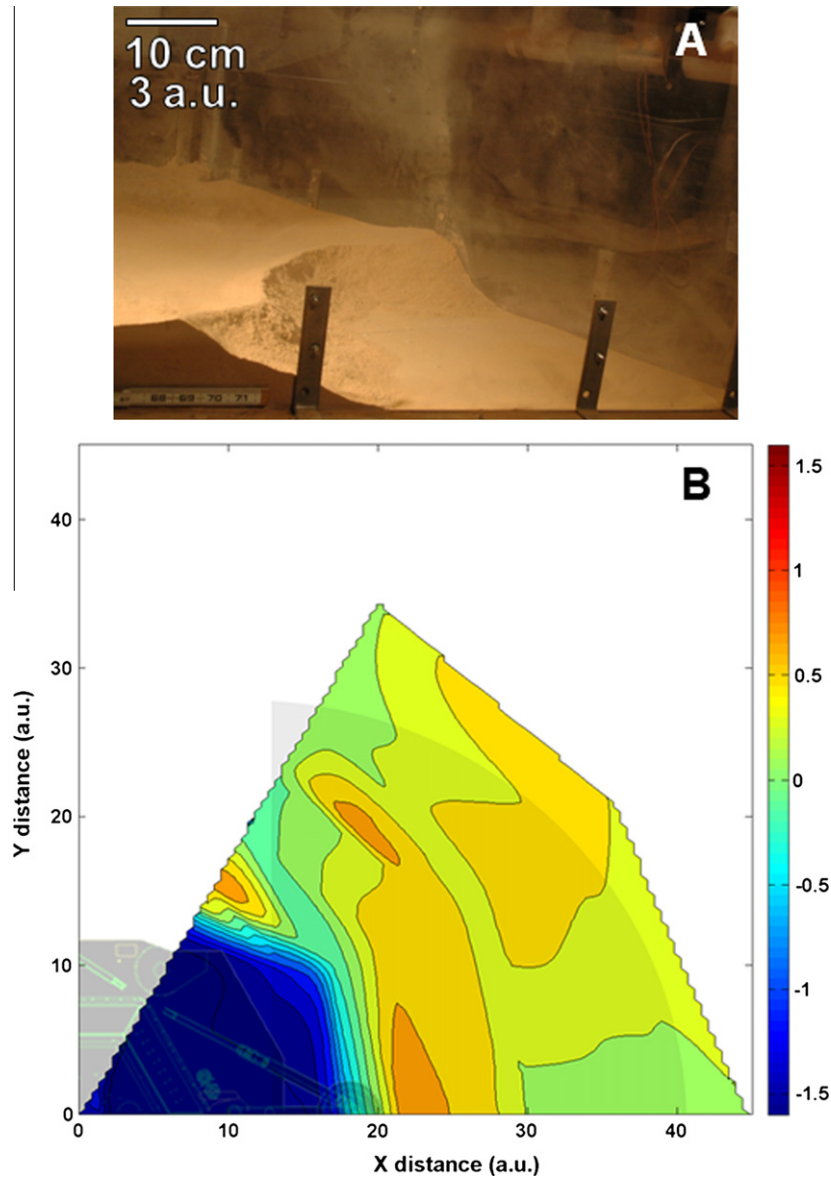


**Fig. 6.** Diffusive gas explosive erosion. (A) Image of the crater caused by Test 2 (Table 5). (B) Normalized erosion/deposition contour plot for crater shown in the above figure; similar contours observed for Test 1. Colorbar indicates the normalized depth of soil in which zero a.u. is the reference value prior to jet impingement. Scaled 90° section of the lander and RA coverage area is indicated in dark shading within the figure. (For interpretation of the references to color in this figure legend, the reader is referred to the web version of this article.)

quantities are calculated by Eq. (11) and denoted in parenthesis or otherwise stated.

$$[x]_{fs} = \frac{D_{fs}}{D_{exp}} [x]_{exp} \quad (11)$$

$[x]$  = length scale quantity

These contour plots indicate that layers of mixtures of fine silt and sand of 5 cm of thickness are completely removed in less than 1 s by DGEE at the scaled Phoenix touchdown altitude of 0.26 m (0.5 m at full-scale), leaving a completely exposed impermeable subsurface with radius of  $\sim 42$  cm (85 cm at full-scale) as illustrated in Fig. 6B (Test 2). In contrast to BCF, DDF and VSE processes, this rapid and broad excavation to the surface occurred in experiments at Mars atmosphere with fine sand (Test 9, Fig. 7A), silt (Test 22, Fig. 8) and their mixtures (Test 1) with depths ranging from 5 to 20 cm. In many cases, the final crater radius exceeded 85 cm in tests with the largest soil depths.

#### 4.2. Predictions at the Phoenix landing site

Through these analyses, we predicted that the subsurface ice could be extensively exposed by this ‘explosive erosion’ process due to pulsed rocket plume–soil interactions prior to Phoenix touching down on the martian arctic (Mehta et al., 2008). As a result, from heat transfer analysis, the subsequent hot jet impingement on the subsurface water ice at the Phoenix landing site would melt  $\sim 1$  mm of its top layer, and splash mud with salt under the lander (Renno et al., 2009). This process led to the first direct observation of deliquescence on Mars (Renno et al., 2009). Deliquescence is the absorption of atmospheric water vapor by hygroscopic materials (salts) to form a liquid brine solution. From the calculations shown in Appendix A and the understanding of the rocket combustion process, a total of  $\sim 0.37$  kg of ammonia may have interacted with the subsurface ice during landing.

The ability of DGEE to remove large quantities of soil in a very short time interval could result in the widespread exposure of

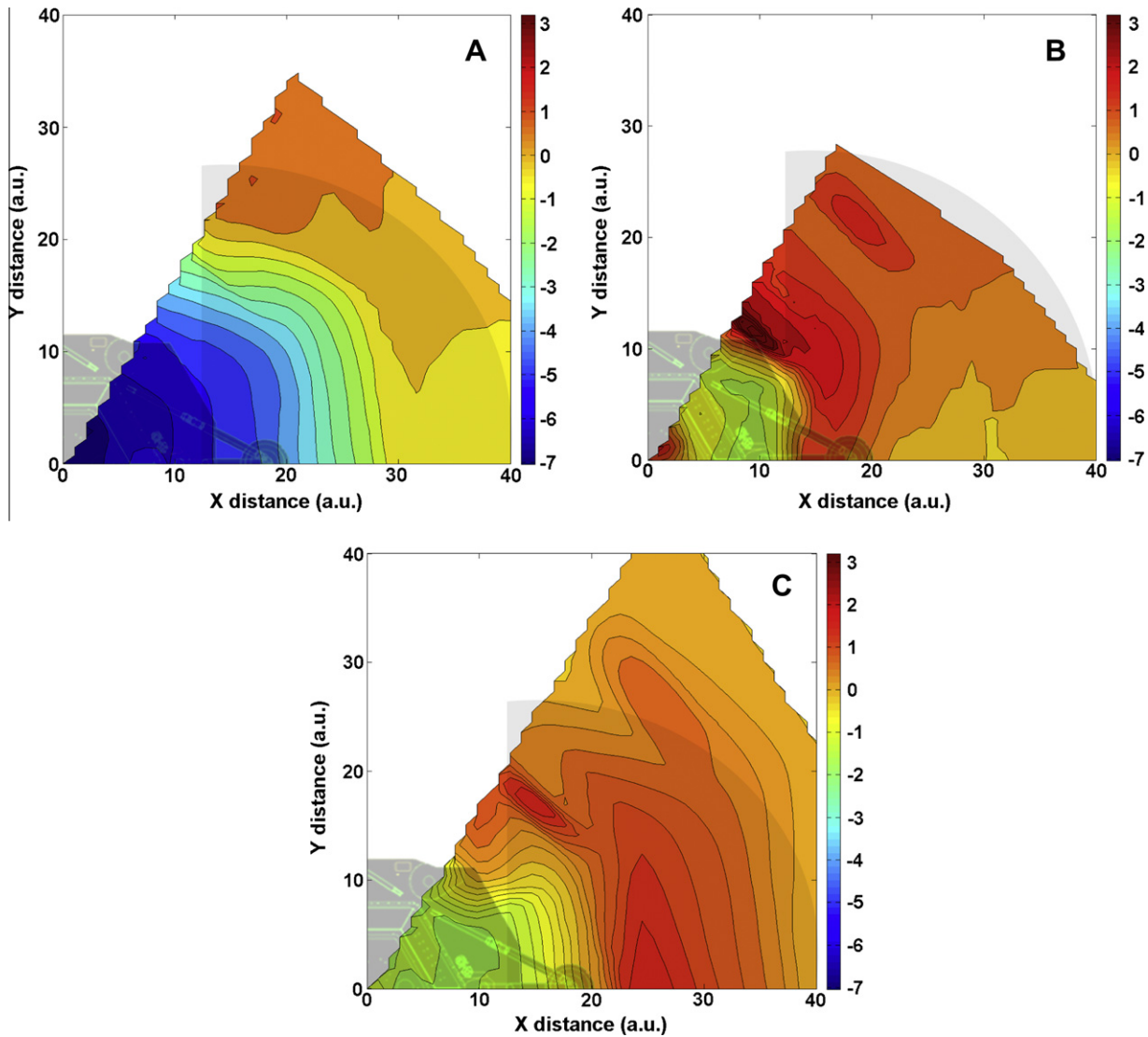


Fig. 7. Normalized erosion/deposition contour plots of laboratory simulations with a 20 cm thick layer of simulant for (A) Test 9, (B) Test 17 and (C) Test 18 (Table 5).

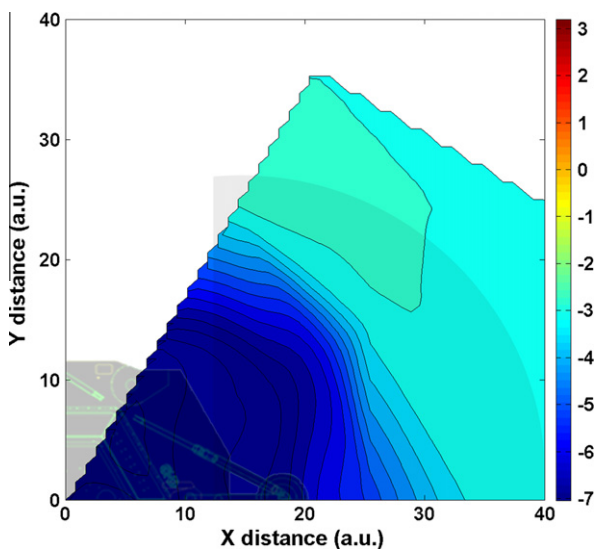


Fig. 8. Normalized erosion/deposition contour plot of laboratory simulation for Test 22 (Table 5).

subsurface ice at the Phoenix landing site as shown by two bright elliptical surface features in the center of Fig. 9. Furthermore, our experimental results indicate that the ‘explosive erosion’ caused by the Phoenix thrusters could remove soil layers with depths in excess of 15 cm, producing a large blast zone by ejecting soil particles meters from the jet impingement point. It also indicates that soil particles removed from below the lander could cover the entire Phoenix work area and beyond with a cm-thick or less layer of loose soil particles as shown in Fig. 6B (Test 2 in Table 5). Our laboratory simulations indicate that if VSE (Fig. 7B is an example of Test 17) or BCF/DDF (Fig. 7C is an example of Test 18) were the dominant erosion mechanisms during Phoenix’s short landing phase, the cratering would be minimal and the subsurface ice would not have been exposed. These claims are further supported by the dynamics of ‘explosive erosion’ and other cratering mechanisms which are presented below.

#### 4.3. Dynamics

Characteristic shock wave structures are readily observed in granular media such as in soil and snow. Granular shock waves occur in nature during avalanches and landslides (Pudasaini and

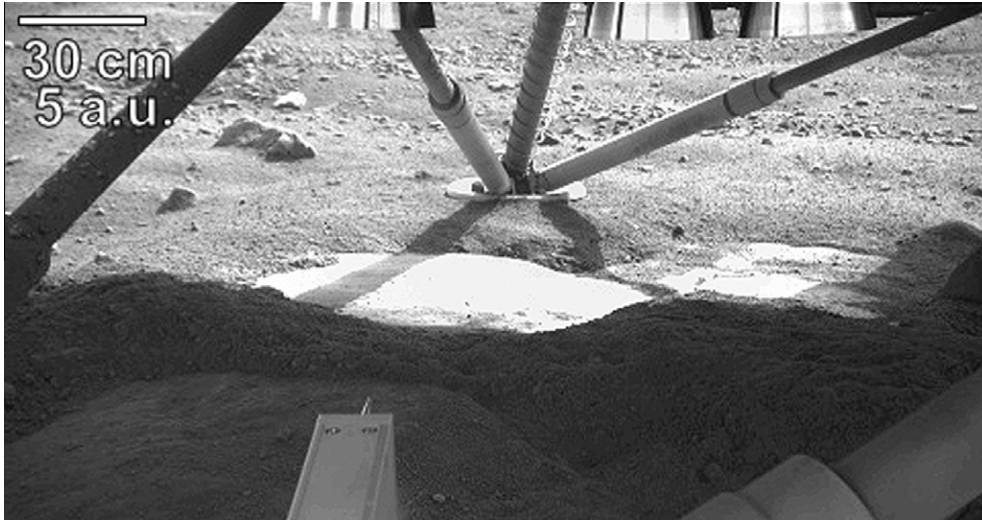


Fig. 9. (B) RAC Sol 5 image (RS005EFF896663219\_11730MDM1) of the extensively exposed ice under the lander near southern footpad (“Holy Cow”).



Fig. 10. High speed images of the ‘explosive erosion’ dynamics observed in Test 9 (Table 5). Images along the  $x$ - $z$  plane (baffle 2) were taken at 500 frames per second using the quarter-space technique. At A2, A4 and A6, three granular shock waves (shown as bright curved granular structures) are observed propagating outward from the impact centerline (epicenter). At A3 and A5, localized soil fluidization (shown as dark semi-stratified regions below the jet) is observed during the thrust shut-down phase. At A7, the exposed surface can be seen, and at A8, minor crater re-deposition occurs. Similar dynamics observed in fine silt/sand simulants (Test 1). See Movie S1.

Kroner, 2008). They occur when high-speed granular flow impinges on obstacles and present similar structure to shock waves in air (Fig. S4, Section 2 of Supplementary material) (Amarouchene et al., 2001). These granular structures also play an important role in DGEE.

The erosion rate of DGEE is much larger than that caused by other erosion mechanisms because it locally fluidizes the soil and produces cyclic granular shock waves as depicted in Movie S1 (Section 3 of Supplementary material) and Fig. 10 (Test 9). These two processes are intimately linked because soil fluidization below the jet plays an important role in the formation and propagation of shock waves. Both of these processes are caused by the short pulse period of the jet relative to the time scale for gas diffusion through the soil ( $\tau/t_{imp} > 1$ ). The ‘explosive erosion’ process is forced by the large pressure variations caused by pulsed cycling of the engine thrust. The partial reflection and collapse of normal shock waves produced by the interaction of pulsed supersonic jets with the surface (Plemmons et al., 2008) augment these variations. Pressure variations at the surface ranging from  $\sim 0.8$  to 40 kPa (Plemmons et al., 2008) forces exhaust gases to penetrate into the porous soil and rapidly diffuse outward because of the low atmospheric pressure,  $\Delta P^* \geq 1$ . Near the end of each engine thrust cycle (thrust shut-down) pressure gradients develop within the soil that causes soil fluidization shown in Fig. 10A3 and A5 as dark mottled bands within the granular media below the jet. This process is described in more detail in Section 4.5.

From Movie S1 during the thrust shut-down phase, we observe the separation of many granular particles from each other along the  $+z$  and  $\pm x$  directions which can lead to the loss of shear strength. This fluidization results in large increases in soil porosity and reduces the speed of sound in it from  $\sim 280$  to  $\sim 0.3$  m/s (Fig. E.1, Appendix E) (Huang et al., 2006; Amarouchene and Kellay, 2006; Liu and Nagel, 1992). From classical continuum-kinetic theory, the speed of sound of granular mediums is dependent on granular temperature and soil volume fraction (porosity). The granular temperature for these systems is much smaller than for gas mediums due to inelastic collisions. The methodology of calculating the sound speed and granular temperature for our application is given in Appendix E.

Cyclic variations in soil porosity create large soil density gradients that produce large variations in the speed of sound (Huang et al., 2006; Amarouchene and Kellay, 2006). This creates super-

sonic and subsonic granular flow regimes when the gas from a subsequent thrust cycle penetrates into the fluidized soil. Granular shock waves, produced during the power rise of each thrust cycle, develop from large pressure gradients between the impingement zone (epicenter) in the fluidized soil interior and its surroundings at  $\sim 800$  Pa. These shock waves, shown as bright radial granular structures in Fig. 10A2, A4 and A6, form and propagate in regions of significantly reduced granular sound speed. Such regions have a low particle density (fluidized) and are shown by Fig. 10A3 and A5 to be relatively darker than the undisturbed areas and semi-stratified.

During the ‘steady power phase’ of the thrust cycle, the pressure of the impinging jet reach high uniform values, compresses the soil, and reduces the pressure gradient between the soil pores in the impingement area and surrounding regions. This increases the speed of sound in the soil and inhibits the formation of shocks fronts (Huang et al., 2006; Amarouchene and Kellay, 2006). As a result, granular shock waves are produced in a cyclic pattern, as indicated by the propagation of high particle density fronts shown in Fig. 10. High speed images show that radial shock waves propagate with an average speed of Mach 12 in relatively high permeability soils. These shock fronts eject a large mass of particles of fine sand and silt ballistically and supersonically with respect to the granular sound speed to  $\sim 3$  m above the surface and at distances greater than  $\sim 4$  m (fine sand) and 15 m (silt) from the wave front. As a result of ejecta with high-kinetic energy, soil deposition occurs over a large area and large accumulations do not occur close to the crater.

High velocity ejecta blankets are produced during the impingement of each jet pulse, until the soil below the thrusters is completely removed. Since the volume of fluidized soil increases with each engine thrust cycle, the radius of the shock waves also expands, leading to increases in the outward flux of ejecta with time. The soil is being ejected and partially re-deposited into the transient crater from surrounding regions during the first four thrust cycles (Test 9). During the fifth thrust cycle, much of the soil has been excavated and re-deposition is minimal, enabling the fluidization depth to extend to the impermeable subsurface. Turbulent entrainment of the granular flow removes the remaining soil. Once the surface is exposed and the nearly final crater has formed, the more benign VSE mechanism begins to dominate the erosion process and removes surface particles along the periphery of the crater and ground topography, producing erosion striations. These

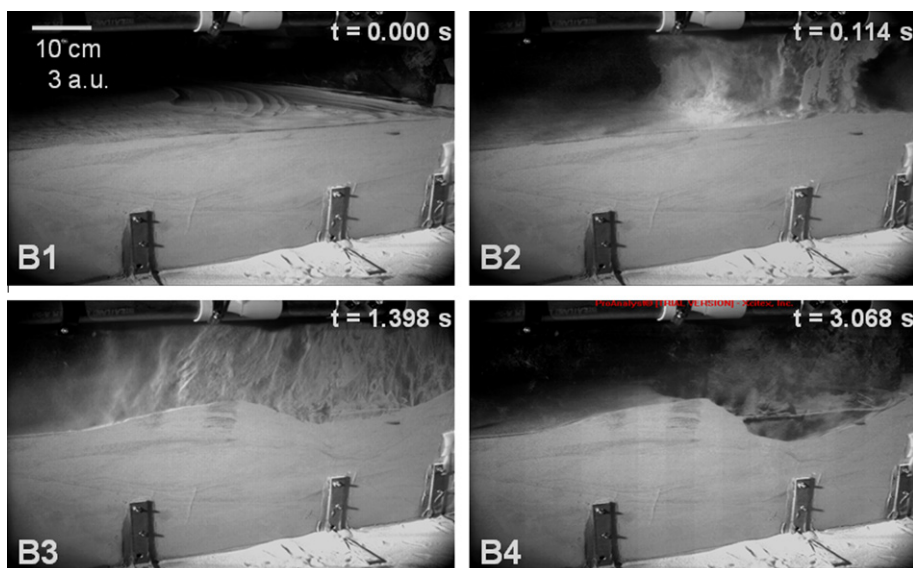


Fig. 11. High speed images of the viscous shear erosion dynamics observed in Test 17 (Table 5). See Movie S2.

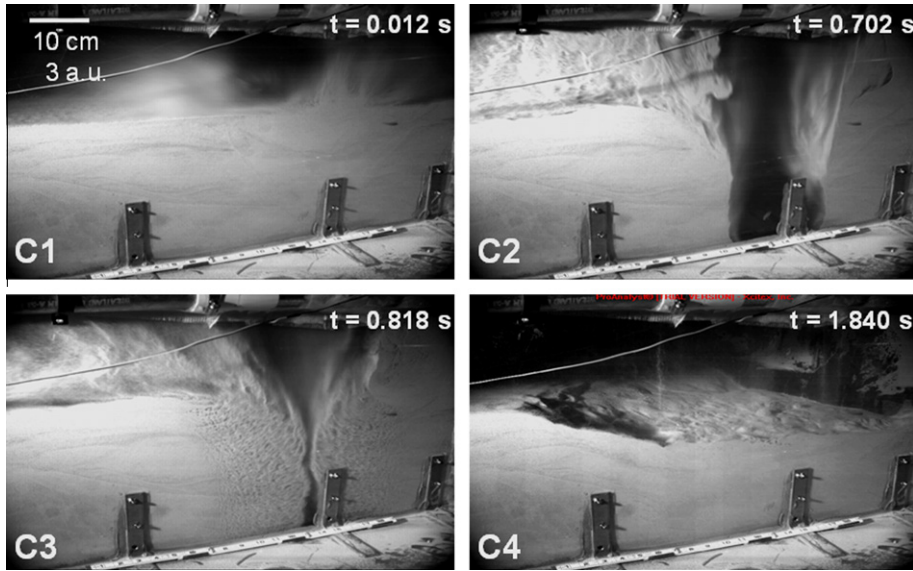


Fig. 12. High speed images of bearing capacity failure/diffusion-driven flow dynamics observed in Test 18 (Table 5). See Movie S3.

dynamics are noted for soil depths between 5 cm and 20 cm, and the number of granular shock waves observed is dependent on the soil depth.

Similar dynamics were observed in experiments with the three soil simulants used in our laboratory experiments: fine sand (Tests 4–11), fine silt (Tests 21 and 22) and fine sand/silt mixture (Tests 1–3). In the experiments with the course sand model (Tests 23 and 24), the dominant erosion mechanism observed was VSE with the formation of a large transient crater and turbulent granular flow. However, in experiments with silt, soil fluidization is more expansive and plays a more important role in the erosion process than in other experiments. Also, the initial radial shock front leads to the ejection of large clumps of silt and turbulent particle entrainment, and as a result subsequent granular shock waves

are either less visible or possess smaller amplitudes. Localized soil fluidization and granular shock waves do not occur in the VSE and BCF/DDF processes as depicted by Figs. 11 and 12, respectively, and therefore they produce smaller and shallower craters. To further elucidate these dynamics, schematic comparisons between DGEE and other jet-induced erosion processes are shown in Figs. S5–S8 of Section 4 of the Supplementary material.

4.4. Quantitative analysis

Next, we quantify the sudden increase in soil density across the shock fronts and the DGEE granular flow physics presented above, using the light reflectance photometry technique (Lee et al., 2007; Caesar-Ton That et al., 2008; Hapke, 2008). The soil volume fraction is calculated from reflectance intensity data provided by the high speed images (Appendix F). A calibration curve is developed, where relative black and white pixels with a pixel length of ~400 μm represents 0 and ~1 soil volume fractions (relative density), respectively (Caesar-Ton That et al., 2008). A calibration curve is specific to different granular media or particle sizes. For Fig. 13 (Test 9), the soil volume fraction data is obtained along the +x-axis on the x–z plane (baffle 2) from the granular shock wave epicenter (x = 28.2 cm) to a radial distance of 15.6 cm (x = 45.6 cm). Similar analyses were conducted for the fluidization regimes within an area band of z = ±0.1 cm. The x-coordinate is fixed at the epicenter for each time interval, but the z-coordinate decreases during the erosion process from z = 17.2 cm at t = 0.112 s to z = 13.2 cm at t = 0.214 s. These profiles of soil volume fraction vs. normalized x-distance as shown by Fig. 13 are calculated at various stages of DGEE along the +x-axis.

Analysis (Appendix F) of sequence of images of the DGEE process in fine sand simulant indicates that the soil volume fraction jumps from ~0.2 to ~0.8 at the beginning of each thrust cycle as shown by the orange and black profiles in Fig. 13, suggesting the formation of a strong shock wave. The images also show that when the soil becomes fluidized near the end of each thrust cycle, the soil volume fraction at the origin decreases from ~0.5 to below 0.2 (granular gas) as illustrated by the red, blue and green curves, substantially reducing the speed of sound in it. It is difficult to quantify subsequent shock waves because of the increased fluctuations in the soil volume fraction (reflectance intensity). With each pulse cycle, the shock strength increases and fluidization further decreases

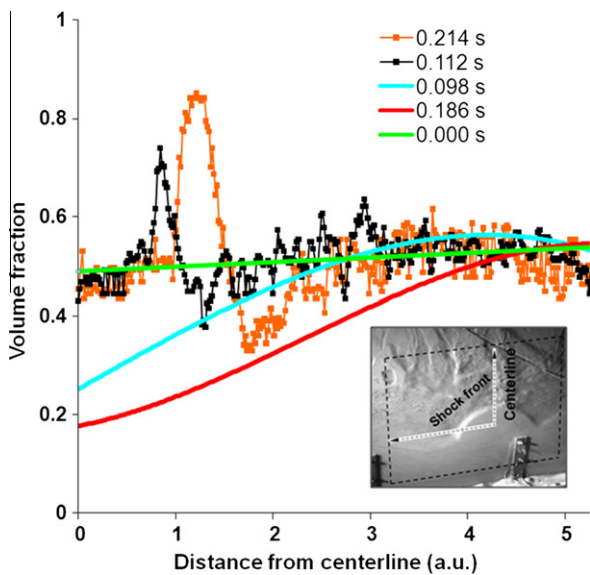


Fig. 13. Soil volume fraction as a function of normalized x-distance from the epicenter of a granular shock wave, at the times indicated in Fig. 10, during the ‘explosive erosion’ process (Test 9). These profiles are calculated from reflectance intensity data. Third order polynomial fitting was used for experimental data at times t = 0.098 s and 0.186 s and linear fitting was used at t = 0.00 s.

the soil volume fraction and expands its domain. Large increases/decreases in the soil volume fraction (density) are not observed in experiments dominated by either BCF/DDF or VSE as illustrated in Figs. 11 and 12.

Our analysis suggests that the uncertainty in the volume fraction value for fine sand simulant (Lee et al., 2007; Caesar-Ton That et al., 2008) is approximately  $\pm 0.05$ . In order to account for small asymmetries in the light illumination angle (leading to small localized bright and dark zones away from the area of interest), we determined the average soil volume fraction profile prior to jet impingement along an area band of  $z = \pm 5$  cm as seen by the green curve in Fig. 13. This analysis suggests a mean volume fraction of  $\sim 0.5$ , which agrees with density measurements for fine sand (Test 9). Light oversaturation of the complementary metal–oxide–semiconductor (CMOS) sensors may record higher reflectance values for the brightest pixels within the image, known as the blooming effect, and specular reflection may result in larger uncertainty values.

The qualitative assessment of granular shock waves shown in Fig. 10 indicates that it also has similar characteristics to shock waves observed in supersonic gas media (Fig. S4, Supplementary material). Dark and bright bands of the shock structure within gas and granular media are observed in all images. Although reflectance intensity profiles and qualitative observations support localized soil fluidization which led to the formation of these shock waves, we numerically and analytically investigate this dominant mechanism caused by DGEE.

#### 4.5. Gas diffusion induced fluidization within granular media due to DGEE

Through analytical calculations, and numerical and laboratory simulations, we show that DGEE can cause gas diffusion to extend to large depths in short time intervals and lead to both localized soil fluidization and formation of granular shock waves. The characteristic diffusion time  $\tau$ , and characteristic one-dimensional diffusion velocity ( $=l/\tau$ ) to depth  $l$  can be calculated from Eq. (7). As described in Sections 4.3 and 4.4, DGEE is not a static process. Indeed, it causes many jet and soil parameters to change by orders of magnitude in short time scales. For example in Fig. 13, the soil volume fraction decreases by a factor of  $\sim 3$  within 0.2 s during this process, significantly increasing the average soil porosity. According to the Kozeny–Carman equation (Eq. (12)) and the assumption of Darcian flow within the granular micro-pore space (Costa, 2006), an increase in  $n$  increases the soil permeability by orders of magnitude. This equation is derived by applying the Navier–Stokes equations within an assembly of capillary tubes representing the pore spaces of the granular media. Eq. (12) and the parameter  $C$ , a function of particle diameter, tortuosity of the pores and shape factor, assumes homogeneous semi-spherical fine sand particles with the same  $\bar{d}$  used in Test 9. This particle size is also similar to the effective particle diameter calculated from Carrier (2003).

$$k = C \frac{n^3}{(1-n)^2}; \quad C = \frac{\bar{d}^2}{180} \quad (12)$$

Due to DGEE, the characteristic diffusion time decreases by a factor of greater than 50 from the maximum values recorded in Table 2 which results in a 1-D diffusion velocity of  $\sim 1$  m/s. Along with large changes in the soil properties responsible for gas diffusion, the ground pressure values significantly change due to the interaction of pulsed jets with the surface (Plemmons et al., 2008). Ground pressure values can transiently increase by a factor of 3–5 times the value at steady state due to partial plate shock formation and collapse at the soil surface. This could further increase the characteristic diffusion velocity to  $\sim 2$  m/s.

From Fig. 10, granular shock wave epicenters originate from  $z = 17$  cm at  $t = 0.112$  s down to  $z = 7$  cm at  $t = 0.318$  s. The shock wave epicenters occur at an average soil depth of  $\sim 4$  cm per thrust cycle. Gas diffusion and large pressure gradients need to develop to these soil depths in order for granular shock wave propagation to initiate at these locations. Hence, the experimental results for Tests 4 and 9 show an average lower bound value of the characteristic gas diffusion velocity to be 0.4 m/s.

Along with the results from the analytical calculations and experimental observations presented above, an axisymmetric time-varying numerical simulation which is more quantitatively accurate shows that gas diffusion by the exhaust plume during the thrust rise phase has the potential to reach large depths within the granular bed in short time scales and initiate soil fluidization during thrust shut-down due to DGEE. The localized fluidization process that occurs during DGEE is dependent on  $\Delta P^*$  and large variations in soil properties. The numerical simulation is conducted with an axisymmetric explicit finite-difference code (Scott and Ko, 1968) based on a second-order non-linear differential equation (Eq. (13a)) with a time-dependent impingement pressure profile. This is developed using MATLAB. We make the assumption that isothermal transient flow within the porous medium obeys Darcy's Law (Eq. (13a)) (Scott and Ko, 1968). This transient numerical model simulates normalized pore pressure contours in a granular bed due to jet interactions with soil depth ( $z$ ) of  $15D$  and radial domain ( $x$ ) of  $15D$  with a time step of  $1 \times 10^{-7}$  s. The pore pressure ( $p$ ) values are normalized with respect to the steady-state jet impingement pressure. The outer walls of the simulations at  $z = 0$  and  $x = 15D$  are modeled as impermeable surfaces where  $x = r$  is the radial component. The axis at  $x = 0$  is defined as the axisymmetric line. For simplicity, we model the pulsed jet from a pair of thruster nozzles as a sine pressure wave (Eq. (13b)) with a pulse width,  $T_{PW}$ , for a single thrust cycle that interacts with a static granular bed with constant permeability and porosity. Hence, the removal of sand grains is not simulated. Prior to jet impact and during the thrust shut-down phase, the model assumes a constant pore surface pressure in equilibrium with the martian atmosphere (Eq. (13b)). Exhaust plume and soil properties used within the simulation shown in Fig. 14 are generally representative of the experiment conditions.

$$\frac{\partial^2 p^2}{\partial z^2} + \frac{1}{r} \frac{\partial}{\partial r} \left( r \frac{\partial p^2}{\partial r} \right) = \frac{2n\mu}{k} \frac{\partial p}{\partial t} \quad (13a)$$

$$\frac{p(t)}{P_{imp}} = 1.0 \sin \left( \frac{\pi t}{T_{PW}} \right) + \frac{P_{amb}}{P_{imp}}; \quad 0 \leq t \leq T_{PW} \quad (13b)$$

$$\frac{p(t)}{P_{imp}} = \frac{P_{amb}}{P_{imp}} = \text{constant}; \quad t > T_{PW}$$

DGEE is a highly dynamic process and as a result, soil permeability and porosity significantly change during a single thrust cycle, but even more so from one cycle to another. Fig. 14 shows the pressure contours within the fine sand simulant (S) at times  $t = 0.015$  s,  $t = 0.030$  s and  $t = 0.085$  s for soil porosities of  $n = 0.50$  and  $n = 0.78$ . This soil porosity implemented in the code simulates the average bounds observed during the DGEE process in the experiments (Tests 4–11) noted in Fig. 13. We observe that the pressure contours can extend to a soil depth of  $\sim 11$  cm with an average soil pore pressure greater than 3.0 kPa at  $t = 0.015$  s (thrust rise phase) for a soil porosity of  $n = 0.78$ . Maximum gas diffusion depth of  $\sim 17$  cm is reached at 0.0325 s when maximum thrust is reached. Hence, this leads to the formation of granular shock waves at martian atmospheric pressures. The pressure contours dissipate to less than  $\sim 2.2$  kPa and expand to a soil depth of  $\sim 34$  cm and radius of  $\sim 38$  cm during the thrust shut-down phase ( $t = 0.085$  s). Higher pore pressure contours of  $\sim 5$  kPa are observed at the start of the thrust shut-down phase ( $t = 0.065$  s). This leads

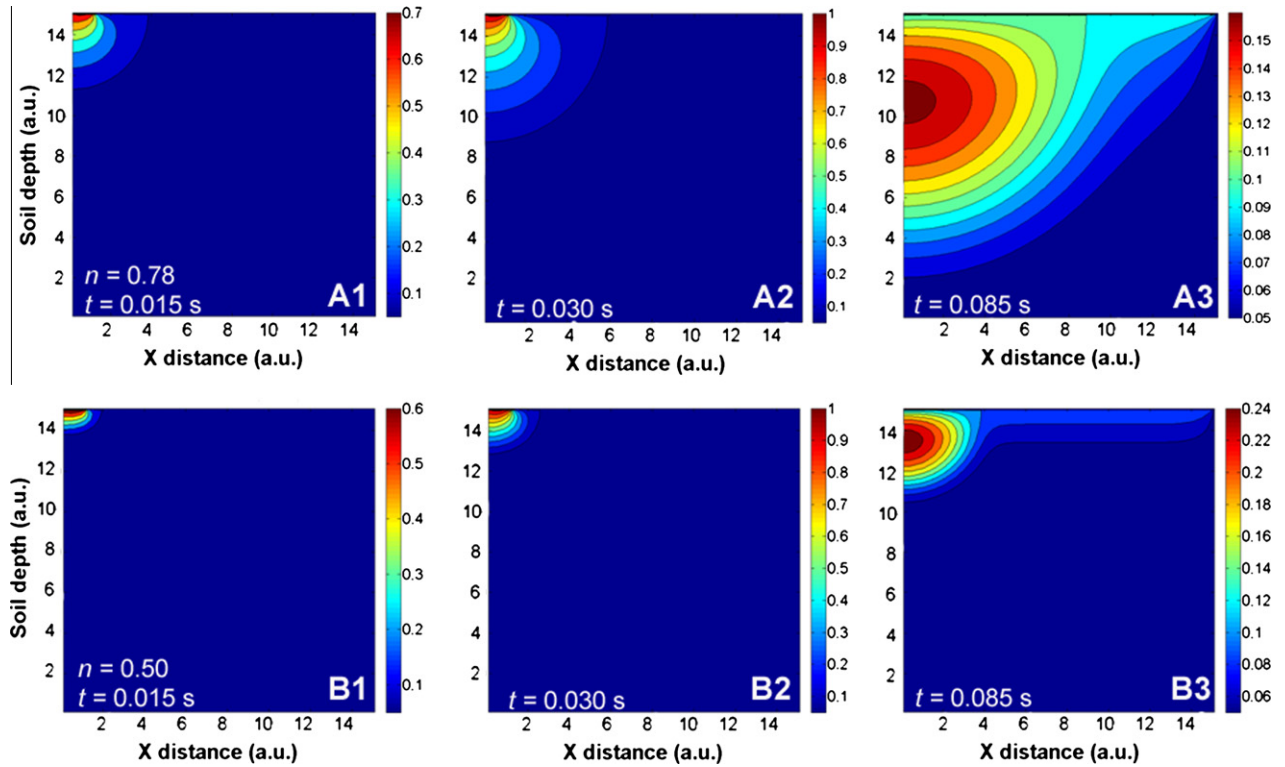


**Fig. 14.** Results of numerical simulations of the time-varying pressure wave propagating within the fine sand simulant for a single thrust cycle at Mars atmospheric pressure for the laboratory simulations (Tests 4–10). All length scales are normalized by the nozzle exit diameter and the colorbar depicts the pore pressure values within the soil which are normalized by the average steady state impingement pressure,  $P_{imp}$ . We show these pressure contours at  $t = 0.015$  s,  $t = 0.030$  s and  $t = 0.085$  s for two average bounds in soil porosity observed experimentally:  $n = 0.50$  and  $n = 0.78$ . (For interpretation of the references to color in this figure legend, the reader is referred to the web version of this article.)

to the pressure gradient forces on the soil particles exceeding the normal atmospheric pressure and cohesive forces. Hence, this process is more readily observed at low atmospheric pressure environments (Mars) than at terrestrial atmospheres.

Once these gradients break minor cohesive bonds, the only restraining force is the cumulative weight of the sand grains. For the particle sizes studied, the pressure gradient force is slightly larger than the particles’ gravitational force during the thrust shut-down phase ( $t = 0.065$ – $0.1$  s), causing the effective stress to be zero and the soil to enter a fluidized state as observed experimentally. For porosities between  $n = 0.5$  and  $n = 0.78$ , the potential fluidization depth,  $z_f$  (Eq. (13c)), which results in soil instability ranges from 10 cm to 16 cm per thrust cycle. This calculation from Eq. (13c) takes into consideration the gravitational weight and cohesive strength of a column of sand of cross sectional area  $d^2$  which extends from the surface to a depth  $z_f$  where the gas diffusion pore pressure can lead to such instabilities. It should be noted that the pressure contours leading to soil instability show relatively good agreement with the fluidization spatial profile shown in Fig. 10A3 and A5.

$$z_f \leq \frac{\frac{3}{2}[p(x, z, t) - P_{amb} - c(t)]}{\rho_p g} \quad (13c)$$

As a comparison, we show that for a constant soil porosity of  $n = 0.5$  during the thrust rise phase, gas diffusion extends to a soil depth of 4 cm with an average pore pressure of 6.4 kPa and expands to a depth of  $\sim 13$  cm with a pore pressure less than 4 kPa during the thrust shut-down phase. Hence, the average characteristic diffusion velocity from these numerical simulations is between 1 and 3 m/s. This is also observed experimentally, where the depth of fluidization and resulting shockwave epicenter are much smaller for the first thrust cycle where the initial porosity is 0.5 as opposed to sub-

sequent cycles. The duration when maximum penetration depth is reached is most likely smaller in our laboratory simulations due to a shorter thrust rise phase than numerically simulated. From conducting a series of numerical simulations with slight variations in permeability and porosity (sensitivity tests), we find that a decrease in soil permeability by a factor of 10 from theoretical values at pre-jet impact conditions has a relatively minor effect on the pressure contour profiles and decreases the calculated depth of gas penetration and fluidization by a factor of  $\sim 0.7$ .

As a further comparison, the numerical model was applied to input conditions from the full-scale Phoenix REM thrusters and soil properties typical of Mars as shown in Table 2. Hot fire test data of the REM motors were used to bound the simulations shown in Fig. 15. Here, the maximum diffusion depth reaches  $\sim 16$  cm at  $n = 0.78$  and  $t = 0.030$  s and then expands to  $\sim 32$  cm during the thrust shut-down phase. Good agreement with numerical simulation results for the subscale experiment was observed for the absolute values of the depth of gas penetration and pressure contours. Normalized jet penetration radius during thrust rise show good agreement between full-scale and subscale results. Inconsistencies in the normalized radius and depth between the two cases are observed during the fluidization regime at the thrust shut-down phase. Slightly higher pore pressure values were predicted for the full-scale case, but it should be noted that the pulse width for the Phoenix REM motors are shorter than for the experiments (Table 1). Gas diffusion depth does not necessarily scale with nozzle diameter as observed for the penetration radius. This predominantly scales with known soil properties and the impingement pressure magnitude and temporal profile.

Overall, the numerical simulations and analytical calculations support the observations seen in Tests 4–10 and that the ‘explosive erosion’ process leads to the formation of granular shock waves,

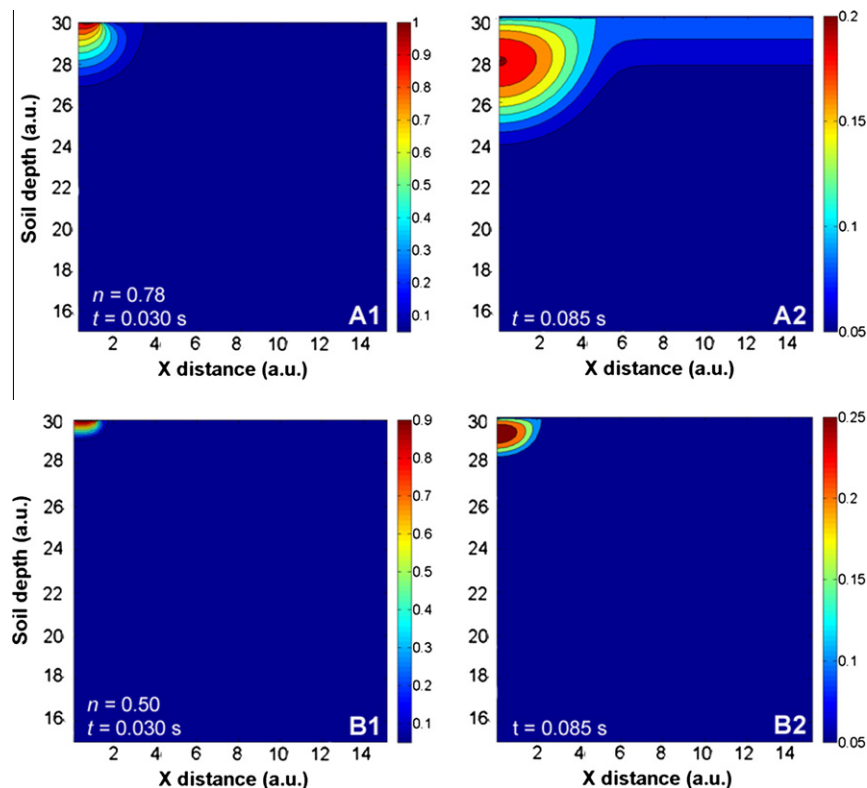


**Fig. 15.** Results of the numerical simulations of the time-varying pressure wave propagating within fine basaltic sand at 160  $\mu\text{m}$  for a single thrust cycle at Mars atmospheric pressure. The input and boundary conditions correspond to the full-scale Phoenix REM thrusters firing during descent.

soil fluidization and large penetrations of the exhaust plumes into relatively fine grained and low cohesive granular media within short time scales. The full-scale numerical simulation also supports that ‘explosive erosion’ was likely the governing mechanism during the Phoenix landing. The smaller grain and higher porosity of the fine silt simulant (Tests 21 and 22) may explain the expansive fluidization during thrust shut-down phases. Another possible but an unlikely mechanism that could have assisted liquefaction is vibro-fluidization, a process in which large surface vibrations could lead to extensive soil fluidization.

Although the assumption that viscous dominant flow within the micro-pore space is reasonable, especially during the thrust shut-down phase and deeper within the soil, there may be times within the thrust cycle and regions within the granular media where inertial effects become important. This increases complexity of the problem, but Teruel and Rizwaan-uddin (2009) show that the permeability for turbulent flows, determined numerically, also increases with soil porosity,  $k = f(n^3/1 - n)$ . Also, modeling of turbulent flow in porous media is limited and there is currently no consistent well founded methodology (Teruel and Rizwaan-uddin, 2009). The Kozeny–Carman equation is well established for applications with granular media larger than clays, but more accurate calculations of the permeability may be obtained by measuring the sphericity factor and tortuosity of the granular media and rigorously accounting for permeability anisotropy and varied particle size distributions.

## 5. Relatively benign jet-induced erosion processes at Earth and Mars atmospheric pressure

### 5.1. Viscous shear erosion

Viscous shear erosion dominates during the impingement of pulsed thruster jets into soils composed of fine sand and silt at

Earth atmospheric conditions depicted in Movie S2 (Supplementary material) and Fig. 11 which is an example of Test 17. It can be seen that VSE mainly acts by removing surface layers of soil particles. The radius and depth of the craters developed by VSE shown by Fig. 7B (Test 17) were three to four times smaller than that caused by ‘explosive erosion’ shown by Fig. 7A (Test 9). After pulsed jet impingement for 3 s or less, the crater developed is less than 5 cm deep and had a diameter less than 20 cm. Similar crater profiles were also observed for VSE at Mars atmospheric conditions (Shorthill et al., 1976a,b; Romine et al., 1973). The crater contour profiles showed relatively little difference between soil simulants tested. The large coarse sand/granules ( $\sim 1500 \mu\text{m}$ ) have more massive particles which also inhibits the ‘explosive erosion’ process. No localized soil fluidization or granular shock waves were observed in VSE dominated processes.

Dust lifting is considerably more localized in VSE dominated experiments at Earth and Mars atmospheric conditions than DGEE (Romine et al., 1973). However, soil deposition due to VSE at Mars atmosphere is less. At Earth atmosphere, Fig. 7B shows a contour plot of a distinct crater rim of  $\sim 15$ – $30$  cm in width ( $\sim 30$ – $60$  cm at full-scale) and a deposition of 7–10 cm layers of soil at the location of the lander footpad. The soil was ejected vertically at a steady rate due to the formation of a parabolic crater as shown in Fig. 11, in contrast to ‘explosive erosion’ which led to sudden dynamic events which ejected granular media outward from the shock wave epicenter. The area covered by ejecta is considerably larger in experiments dominated by ‘explosive erosion’ and this correlates well with what is observed at the Phoenix landing site. In these experiments, many soil particles are ejected well beyond the testbed area.

From particle tracking data, we deduce that there are two reasons for the large differences in the deposition location between the two mechanisms. First, the drag on particles or bulk flow at Earth atmospheric pressures is hundred times larger than for the cases at Mars, significantly decreasing the ejecta velocity. Second,

the mean velocity of shock-induced bulk media is five to seven times larger than for viscous shear-induced flows at martian atmosphere. For example, on the Moon, particles can reach supersonic speeds and travel distances greater than 160 m due to supersonic jet interactions. This was recorded by the Apollo 12 crew when they noticed microscopic craters on the Surveyor 3 hardware due to the sandblasting effects during their lunar landing (Jaffe, 1971).

The main difference between the site-alteration characteristics on Mars and Earth, at a similar thruster inlet pressure, is caused by the fact that the impingement pressure is significantly larger at Mars atmosphere conditions than at Earth conditions (Plemmons et al., 2008; Mehta et al., 2007, 2008; Huseman and Bomba, 2000) as shown in Table 5. This occurs because the thruster jet is moderately under-expanded ( $e \sim 4$ ) and collimated at Mars conditions and forces the development of a plate shock at the surface (Plemmons et al., 2008). A highly over-expanded shock structure ( $e \ll 1$ ) which rapidly develops into a subsonic turbulent plume is observed in experiments at Earth atmospheric conditions, leading to the inability of a plate shock to develop at the surface (Plemmons et al., 2008; Mehta et al., 2008). The surface impingement pressures at lunar atmosphere have modest values as well due to a highly expansive plume shock structure (Clark, 1970), characteristic of highly under-expanded jets ( $e > 100$ ). This forms a large areal plate shock which distributes the thrust load over a larger area, significantly decreasing the ground pressure and producing minimal site alteration as observed for previous Apollo and Surveyor missions (Christensen et al., 1967; Mason, 1970).

## 5.2. Bearing capacity failure and diffusion-driven flow

Bearing capacity failure and diffusion-driven flow dominate the erosion process in experiments with steady jets at Mars atmospheric conditions depicted in Movie S3 (Supplementary material) and Fig. 12 which is an example of Test 18. In this case shown in Fig. 12, a partially reflected plate shock developed at the surface, and the soil composed of fine sand simulant was excavated down to the impermeable subsurface in less than a second. Minor eroded soil was ejected away, and upwards by flow deflected by the steep parabolic crater with a diameter of  $\sim 10$  cm.

Diffusion-driven flow drives the soil in a tangential direction and bearing capacity failure forces the soil in a perpendicular direction to the crater surface (Metzger et al., 2009a,b). DDF occurs when the exhaust plume diffuses into the soil layer and through viscous drag removes a uniform soil layer along the periphery of the crater wall. In contrast to DDF, the BCF mechanism alone does not erode soil layers. The pressure force of the jet mechanically compresses the soil, forming a cup-like crater. Majority of the soil is seen to be compressed along the cavity by bearing capacity failure similar to that observed during initial simulations of the Viking and Mars Science Laboratory landings on Mars (Romine et al., 1973; Mehta et al., in preparation). The distinction between which erosion process dominates is determined by the ratio of simulant particle to plume diffusion velocity. If the plume diffuses faster than the movement of simulant grains, DDF prevails and vice versa for BCF (Metzger et al., 2009a,b). We have not assessed in this paper which distinct process between DDF and BCF is governing, but we believe that both processes play a role in erosion by steady jets.

After engine shut-down, most of the eroded and compressed soil rapidly refills the cavity and hence, we hypothesize that BCF was dominant. From Movie S3, DDF was observed near the end of crater formation stage where a diffuse band of soil ( $< 1$  cm in thickness) moves tangentially to the crater as shown in the schematic of Fig. S7 (Supplementary material). The final crater was less than 5 cm deep with a diameter of 50 cm shown in Fig. 7C. Small amounts of viscous erosion were also observed at the outer areas of the crater. Although soil deposition thickness was greater for VSE, loose soil

deposition also surrounds the crater rim for the BCF/DDF process. Similar erosion dynamics and crater profile were observed for the fine silt/dust simulant and this was also recorded for pre-Viking site-alteration experiments conducted with lunar nominal soil ( $d < 20 \mu\text{m}$ ) (Romine et al., 1973). No localized soil fluidization or granular shock waves were observed in experiments dominated by BCF/DDF. Since various jet-induced erosion mechanisms have been experimentally studied at Mars atmospheric conditions, we apply these studies to observations at the Phoenix landing site.

## 6. 'Explosive erosion' at the Phoenix landing site

The idea that DGEE occurred during the landing of the Phoenix spacecraft is supported by images from the Surface Stereo Imager (SSI) and Robotic Arm Camera (RAC) (Smith et al., 2009). These images shown by Figs. 9 and 16 suggest that the erosion removed layers of regolith, rapidly exposing the subsurface ice over a large area (Smith et al., 2009) of  $\sim 2 \text{ m}^2$  and ejecting  $\sim 300\text{--}120$  kg of soil in less than 2 s, as predicted by DGEE. The calculated normalized erosion rates ( $\frac{m_c}{m}$ ) for type B and S simulants with depths between 5 cm and 20 cm at various altitudes (Tests 1–11) range from 20 to 65 for DGEE dominant processes, 40 to 130 when including the mass correction term discussed in Section 2.2. In contrast, these average erosion rates are below 10 (20 by including the mass correction term) for BCF, DDF and VSE processes (Tests 12–20). The range of normalized erosion rates calculated from RAC images of the Phoenix landing site (Appendix A) are between 35 and 100 which are in good quantitative agreement with the laboratory simulations governed by DGEE.

Furthermore, the exposed ice table seen at the southern footpad in Fig. 9 extends to a radius between 75 and 85 cm from the spacecraft centerline with a width of  $\sim 1.1$  m, similarly observed by the 'explosive erosion' process through normalization in applying Eq. (11). In Fig. 9, there are three large patches of the exposed subsurface where two exposed surfaces are bright and the third is much darker. Mellon et al. (2009) indicates that the two bright features are either lighter-toned water ice or ice-saturated soil observed at a high phase angle. They are separated with a modest amount of dark soil deposit. Fig. 16A shows that the ice table was also extensively exposed near the eastern footpad.

In contrast to VSE and BCF/DDF, DGEE produces poorly defined and narrow crater rims with minor fluidized deposition, similar to those observed below the Phoenix lander. Loose soil particles are observed along stagnation planes between the three groups of thrusters and at the spacecraft centerline, in agreement with the design and results of our experiments. Modest amounts of particle deposition are observed around the crater rim, seen by the ejecta-covered rocks near the footpad (Fig. 16D). Our experiments suggest that a layer of loose soil of  $\sim 1\text{--}2$  cm of thickness was deposited in this region located in the work area as indicated in Figs 6B and 7A. This agrees with the fact that the forces on the Robotic Arm indicate less cohesive top soil near the crater rim than in places farther away (Arvidson et al., 2009). Most importantly, these erosion characteristics are further corroborated by our experiments which simulates the dynamic pulsed nature of the impinging jets on soil at Mars atmospheric pressure as observed during the Phoenix landing.

Both local and macroscopic erosion were observed at the landing site. Displaced and ejected pebbles and large-scale rocks (Fig. 16B), ejecta-covered rocks (Fig. 16C), and radial erosion striations all up to 3 m away from the lander centerline (Fig. 16C and E), soil disturbance at a diameter of more than 40 m around the lander (Smith et al., 2009) (Fig. 17) and ejecta deposition even near the top of the legs struts (Renno et al., 2009) are consistent with the explosive nature of DGEE. Some embedded rocks were dislodged from the ice table (Sizemore et al., 2009) due to the jets rapid,

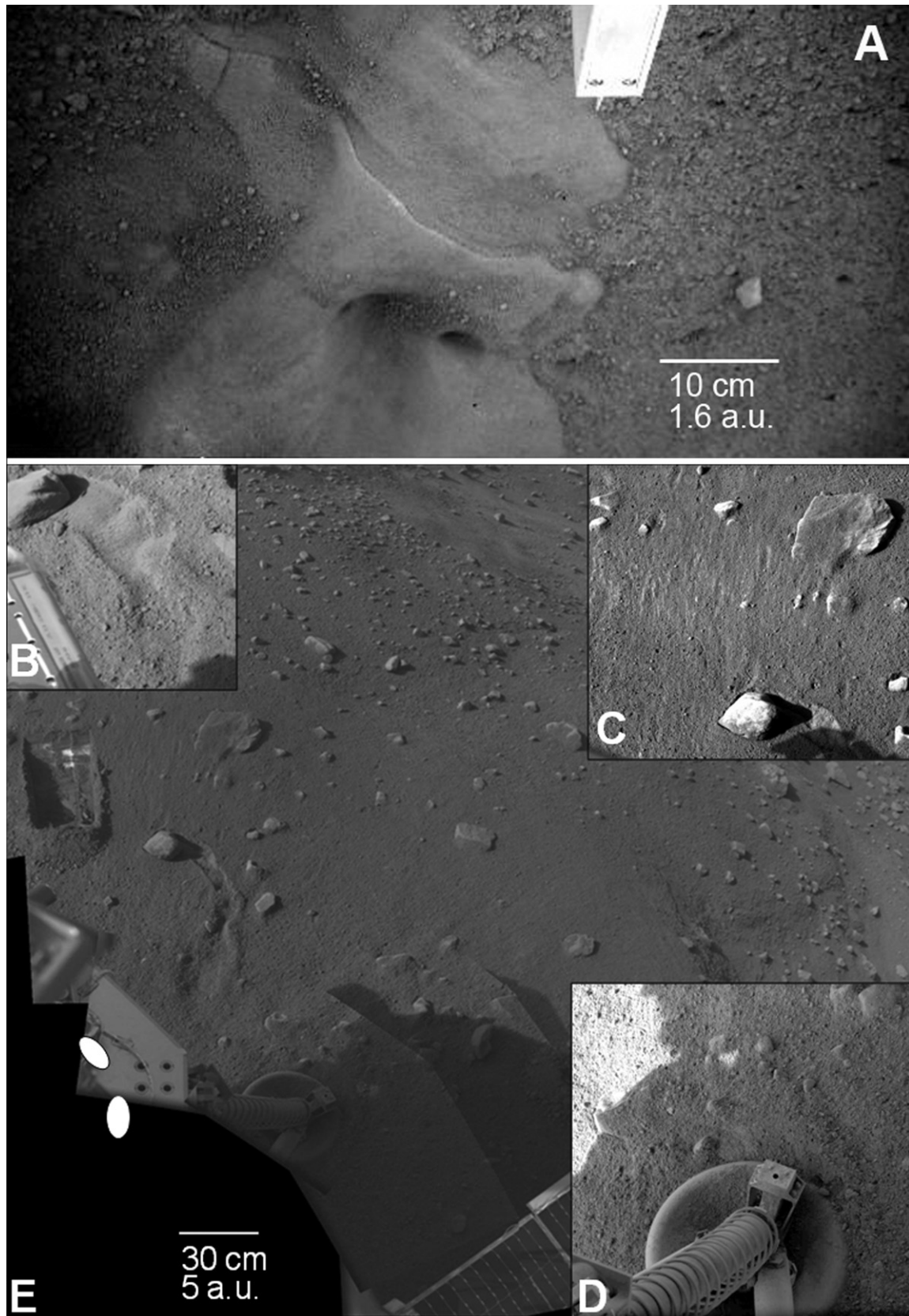


**Fig. 16.** Images of erosion and deposition areas. (A) Close up view of the exposed ice table “Snow Queen” which is approximately  $\sim 55$  cm in diameter (RS006EFF896752928\_117A6MDM1). (B) Sol 7 SSI image (SS007EFF896839472\_117FER1M1) of a rock (of  $\sim 12$  cm of diameter) that was dragged for  $\sim 35$  cm due to the shear force of the exhaust plume. (C) Sol 6 SSI image (SS006EFF896755404\_1179ER1M1) of striations, ejected pebbles, and ejecta-covered rocks out to  $\sim 3$  m from the spacecraft centerline. (D) Sol 0 SSI image (SS000EFF896228288\_10C96R1M1) of loose fluidized regolith is observed near the lander footpad. (E) Sol 5 SSI mosaic of the site alteration features seen with respect to the thrusters (marked in white ovals).



**Fig. 17.** Sol 0 MRO HiRISE image (PSP\_008591\_2485) of the Phoenix landing site taken 22 h after landing. A dark halo of more than 20 m in radius can be seen around the spacecraft depicted by a blue dot. (For interpretation of the references to color in this figure legend, the reader is referred to the web version of this article.)

violent and broad excavation process and high surface impingement pressure loads (Plemmons et al., 2008). These soil disturbances are much larger than those from the Viking, Surveyor and Apollo landings (Shorthill et al., 1976a,b; Christensen et al., 1967; Mason, 1970), and experiments governed by either the VSE or BCF/DDF mechanisms which produced less intense, more localized erosion.

VSE at the Phoenix landing conditions would lift soil particles less than 7 m away from the lander as shown by analytical calculations presented in Appendix C. However, Mars Reconnaissance Orbiter (MRO) High Resolution Imaging Science Experiment (HiRISE) image in Fig. 17 shows a dark symmetric halo extending more than 20 m away from the lander, probably caused by surface erosion due to the impact of sand grains ejected by ‘explosive erosion’ (Smith et al., 2009; Greeley, 2002; Greeley et al., 1974). Another interpretation of this halo is that the high-energy ejecta composed mainly of silty-sand and aggregates could have been deposited over these distances (Markiewicz et al., 2009; Greeley et al., 1974) as observed experimentally. It should be noted that this dark halo was not observed at the landing site prior to Phoenix touching down. Both interpretations support the idea that ‘explosive erosion’ was dominant. Relatively smaller in scale, asymmetric erosion was observed by the backshell and heatshield’s oblique impact with the martian surface, which may imply that the dark halo around Phoenix is characteristic of the “erosion-supported” hypothesis.

Slight discrepancies in the normalized erosion rates and crater profiles between spacecraft observations and laboratory simulation may be due to the assumptions made in our analyses of the

Phoenix data. Calculation of the soil removal from Phoenix data (Appendix A) is under the assumption that the soil media has a relatively constant bulk density and the third group of thrusters exposed a similar fraction of subsurface ice. Since a digital elevation map has not been created under the lander, this value is only an approximation based on limited images taken from Phoenix’s RAC. Also, complete similarity between subscale terrestrial and full-scale planetary processes is difficult to achieve for granular processes and this may lead to some inconsistencies.

## 7. Bulk physical soil properties derived from DGEE

The erosion processes described above can be used to determine approximate bulk physical properties of the soil at the landing site because crater morphology depends strongly on soil porosity, permeability and cohesion (Shorthill et al., 1976a,b; Hutton et al., 1980). Thus, the value of these important soil parameters can be determined by the analysis of images of the area below the lander and its surroundings (Shorthill et al., 1976a,b; Hutton et al., 1980). Our analysis in Appendix C compares the ratio of average volume eroded with that of unaltered soil up to a distance of  $40D$  from the lander centerline between experiments (Tests 1–11 and 21–24) and observations at the workspace region of the Phoenix landing site. This eroded volume fraction has been defined as the crater volume ratio. The average crater volume ratio caused by the Phoenix landing is  $\sim 0.10$ . These calculations based on Figs. 7A, 8 and 18 were averaged between soil depths of 5 cm and 20 cm. DGEE on soils composed solely of fine silt (Tests 21 and 22), which has the highest porosity and lowest permeability of all soil simulants used, predicted to remove greater than six times the volume eroded during the Phoenix landing, corresponding to an exposed area of ice six times larger than observed under the spacecraft (Table 3). Relatively incompressible simulant such as large coarse sand/granules (Tests 23 and 24) or heavily cemented soils are not subject to DGEE and therefore cannot produce the alteration observed at the landing site (Table 3). A mixture of approximate equal parts of fine sand and silt simulant by volume (type B) produces erosion similar to that caused by Phoenix (Tests 1 and 2, Table 3).

First order comparison of the crater volume ratio from our laboratory simulations and that calculated with the Phoenix data suggests that the permeability coefficient and porosity of the soil of the Phoenix landing site are within the range of  $\sim 3 \times 10^{-4}$  cm/s and  $\sim 0.45$ , respectively. The martian arctic regolith seems to possess high compressibility at relatively high pressure loads as discussed in Section 4. These values and general properties can be used to constrain models of hydrological and vapor diffusion

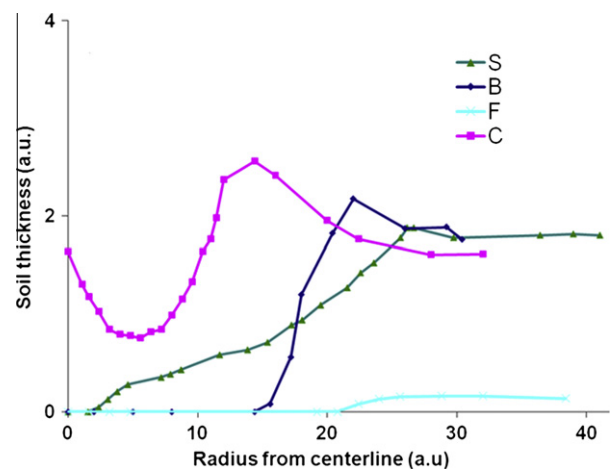


**Fig. 18.** Crater profiles for 5 cm soil depth cases for Tests 2, 11, 21 and 23 (Table 5).

processes and therefore provide insights into the deposition and mobilization of water ice on the martian arctic (Hanna and Phillips, 2005; Sizemore and Mellon, 2008).

From our experimental results and RAC and SSI imaging, the large volume of exposed subsurface water ice, the lack of soil deposition within the crater, and the steep crater walls indicates that the soil at the landing site is a cohesive mixture of fine silt and sand. Since the average crater volume ratio at the landing site is smaller than that observed in laboratory simulations for type-B simulant, the soil cohesive strength may be larger than 3.5 kPa. We hypothesize that duricrust formed by liquid brines may be a source for the higher cohesion (Renno et al., 2009).

As an alternative or in conjunction hypothesis, the crater volume ratio (Table 3) which shows a general increase with decreasing particle size may also imply a larger presence by volume of fine sand ( $d > 200 \mu\text{m}$ ) at the Phoenix landing site than estimated previously by the Microscopy, Electrochemistry and Conductivity Analyzer's (MECA) Optical Microscope (OM) (Goetz et al., 2009). The MECA OM shows two main particle size distributions at the landing site:  $\sim 70\text{--}100 \mu\text{m}$  and  $< 15 \mu\text{m}$ . However, caution must be taken in this comparison because the OM does not sample particles larger than  $200 \mu\text{m}$  in diameter, and therefore its analysis is biased towards a smaller size distribution (Goetz et al., 2009). The presence of a dark halo around the lander (Fig. 17) may also suggest a larger fraction of sand, coarser than the surface deposit which has a higher albedo (Smith et al., 2009; Greeley et al., 1974).

## 8. Conclusions

This study used Phoenix spacecraft data and experimental and numerical simulations to investigate the dynamics of erosion caused by the thruster plume interactions with the soil during the Phoenix spacecraft landing on the martian arctic. Its main results are:

- (1) A new erosion process termed diffusive gas explosive erosion (DGEE) is discovered. DGEE is caused by supersonic pulsed jets impinging in porous soils in tenuous (Mars) atmospheres. The explosive nature of this erosion process is caused by the localized fluidization of soil and the formation and propagation of cyclic and radial granular shock waves. This leads to erosion rates which are 5–20 times greater than that of previously known processes caused by impinging jets. From theoretical calculations, numerical simulations, high-speed imaging and photometry techniques, we are able to qualitatively and quantitatively determine the formation and effects of fluidization and granular shock waves on the surrounding granular media at extreme conditions.
- (2) RAC, SSI and HiRISE images of the landing site, together with our results suggests that DGEE is responsible for the removal of 5–18 cm thick layers of soil, the first discovery of the expansive exposed ice table under the lander and an altered ground morphology that extends to 40 m in diameter which all occurred during the Phoenix landing. The more interesting observation is that this excavation took place in very short time scales of less than a second. This violent erosion process led to the discovery of the first direct evidence of liquid saline water on Mars (Renno et al., 2009) and provided information in regards to site contamination. While surface erosion during previous soft landings on Mars was dominated by VSE (Shorthill et al., 1976a,b; Hutton et al., 1980), we show the erosion during the Phoenix landing was dominated by DGEE.
- (3) Through experimental findings and spacecraft imaging of the altered landing site, we are able to approximately quantify through interpolation the various soil properties of the martian arctic plains that can be determined through jet-induced erosion.

The main goals of this research are twofold: (i) predict the extent of erosion and deposition at the Phoenix landing site due to the spacecraft landing phase and (ii) provide insights into the behavior of granular media subject to thruster jet interactions at martian atmosphere. Through these analyses, the extent of erosion and deposition was accurately predicted at the Phoenix landing site prior to the spacecraft touching down. Based on past studies on scaling laws, this paper takes a fresh look at the scaling of jet–soil interactions. Accurately simulating the dynamics of granular flow as attempted here should be paramount and a first step in understanding these interactions. Most importantly, the physics described in this paper sheds light into the dynamic behavior of granular media subject to jet impingement at extreme conditions of low atmospheric pressure and low gravitational acceleration.

This study may also provide important information into in situ resource utilization (ISRU) technology. This highly efficient and extremely rapid erosion process could be used to excavate the soil and extract resources from it. Pulsed cold gas thrusters on the spacecraft can be used as a low cost instrument to effectively sample martian soils.

Additional experiments at low atmospheric pressure environments with large variations in particle sizes and densities and plume velocities are necessary to validate the scaling laws and further corroborate our theories of jet-induced erosion processes at extreme conditions. Along with additional terrestrial experiments, it would be beneficial to conduct a series of controlled tests on Mars, of the effect of supersonic jets on granular soil. This can provide ground truth to both the discussed scaling laws and more importantly to numerical models being developed. Although limited, similar tests in the 1960s were conducted using NASA Surveyor V's liquid propulsion system on the Moon. Numerical models in conjunction with laboratory simulations are essential in fully characterizing these complex interactions. For future manned and robotic missions to Mars and other celestial bodies, the understanding of these interactions is critical for the safety and survivability of the crew and spacecraft. Although the engineering applications and granular flow physics of 'explosive erosion' are important, this discovery led to a revolutionary thinking in the search for life on Mars (Renno et al., 2009).

## Acknowledgments

We thank R. Gillespie, R. Greeley, C. Woosley, P.G. Huseman, D.S. Gulick, G.L. Romine, E. Bailey, R. Hryciw, J.T. Heineck and Y. Jung for contributing to this study. The authors would like to recognize the extensive efforts by the Phoenix Entry, Descent and Landing and Science teams that made this mission a success. We also acknowledge the support of NASA's Planetary Geology and Geophysics Program for providing operational costs for the ASU-NASA Ames Planetary Aeolian Laboratory. We would also like to thank P.T. Metzger of NASA Kennedy Space Center and other anonymous reviewers for the critical evaluation of the manuscript. This research was supported by the Phoenix Mars mission, the Michigan Space Grant, and by Lockheed Martin Corporation. M. Mehta was supported by NASA's GSRP Grant NNX06AH56H.

## Appendix A. Calculations of crater dimensions and ammonia contamination at the Phoenix landing site using RAC images

The radius of exposed ice under the lander was estimated by the analysis of RAC images using the centerline  $-Y$  (eastern) footpad coordinates of the Phoenix spacecraft as a reference. These coordinates were provided in the Payload Frame (Eq. (A1)) which was converted to Lander Centerline Frame (Eq. (A2)). By observing images of "Snow Queen" (Fig. A.1) which showed the outer portion of the exposed ice, we were able to approximately assess the distance between the outer exposed ice and the  $-Y$  footpad edge. This

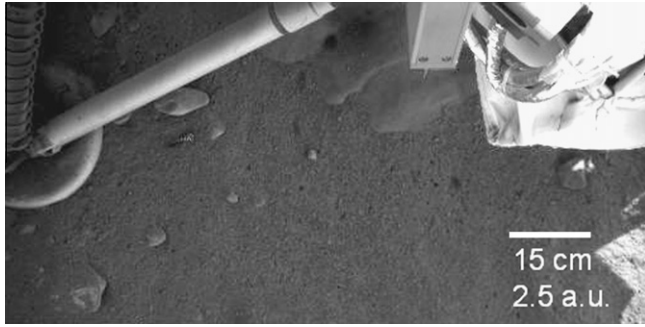


**Fig. A.1.** Subsurface ice, “Snow Queen”, shown exposed below the lander near the eastern footpad (RS005EFF89662260\_11736MDM1).

distance scales from 1.2 to 0.9 footpad diameters ( $d_{\text{footpad}}$ ). As a result by applying Eq. (A4) and estimating the radius of soil deposition near the centerline of the spacecraft ( $r_{cl}$ ) (Fig. 9), the ice exposed by the rocket plume impingement spans a length in the  $-Y$  direction,  $L_c$ , between 65 and 55 cm. Approximating that a crater with an elliptical profile was produced per every four descent thrusters (Fig. 9), the crater dimensions and other parameters such as its perimeter ( $p_c$ ), semi-major length ( $a_c$ ), semi-minor length ( $b_c$ ), volume ( $V_c$ ) and mass of total ejecta ( $m_c$ ) were calculated by applying Eqs. (A6)–(A9) to known quantities such as the crater depth and angle of repose ( $\theta_r$ ). Although soil depths greater than 10 cm have been recorded within Phoenix’s workspace, the average depths between 5 cm and 10 cm were used in these calculations. It should be made clear that these are approximations generated from limited RAC images. No adequate DEMs were created to confirm these values. By knowing the time during descent when ground effects begin until touchdown of the spacecraft,  $t_L$ , the average normalized erosion rate (Eq. (A10)) estimated from the Phoenix landing site is between 35 and 100.

$$\begin{aligned} & -Y \text{ footpad centerline in payload frame : } [x, y, z]_{\text{payload}} \\ & = [7.4, 53.6, 107.0] \text{ cm} \end{aligned} \quad (\text{A1})$$

$$\begin{aligned} & -Y \text{ footpad centerline (FC) in lander frame : } [x, y, z]_{\text{lander}} \\ & = [60.8, 107.0, 123.1] \text{ cm} \end{aligned} \quad (\text{A2})$$

$$\begin{aligned} & \text{Lander centerline (LC) in lander frame : } [x, y, z]_{\text{lander}} \\ & = [0.0, 0.0, 123.1] \text{ cm} \end{aligned} \quad (\text{A3})$$

$$R = \sqrt{(x_{LC} - x_{FC})^2 + (y_{LC} - y_{FC})^2 + (z_{LC} - z_{FC})^2} + \frac{d_{\text{footpad}}}{2} \quad (\text{A4})$$

$$L_c \sim R - 2d_{\text{footpad}} - r_{cl} \quad (\text{A5})$$

$$p_c \sim \frac{4}{3} \pi (R - 2d_{\text{footpad}}) \quad (\text{A6})$$

$$a_c = \frac{L_c}{2}; \quad b_c \sim \sqrt{\left(\frac{p_c}{\pi}\right)^2 \frac{1}{2} - a_c^2} = \frac{1}{6} \sqrt{32(R - 2d_{\text{footpad}})^2 - 9L_c^2} \quad (\text{A7})$$

$$V_c \sim \pi a_c b_c h + \frac{\pi h^2}{2 \tan(\theta_r)} \left( \frac{h}{\tan(\theta_r)} + a_c + b_c \right) \quad (\text{A8})$$

$$m_c \sim \rho_p n V_c \quad (\text{A9})$$

$$\frac{\dot{m}_c}{\dot{m}} = \frac{m_c}{t_L \dot{m}} = \text{normalized erosion rate} \quad (\text{A10})$$

The total mass of ammonia,  $m_{\text{NH}_3}$ , that may have interacted with the ice surface due the Phoenix landing propulsion system was determined based on a pair of thrusters’ exhaust properties such as the mass flow rate,  $\dot{m}$ , and mass fractions,  $f$  (Eq. (A11)). The mass fraction of ammonia of 0.49 was determined from the Phoenix hot thruster firing tests performed in a vacuum chamber at Mars atmospheric conditions (Plemmons et al., 2008). The  $t'$  is the time differential between  $t_L$  and the time to expose the subsurface ice ( $<1$  s).

$$m_{\text{NH}_3} = 6\dot{m}f_{\text{NH}_3}(0.45t') \quad (\text{A11})$$

## Appendix B. Jet–soil interaction dimensional analysis

Buckingham–Pi dimensional analysis theory (Buckingham, 1914) was used to obtain dimensionless parameters given the important input conditions needed for describing jet–soil interactions. A jet with velocity,  $U$ , density,  $\rho_a$  and viscosity,  $\mu$ , exhausting from a nozzle diameter,  $D$ , interacts with granular media with a particle diameter of  $d$ , density,  $\rho_p$ , porosity,  $n$ , shear strength,  $Y$ , and depth,  $l$ . The jet of mass flow rate,  $\dot{m}$ , interacts with the granular media for a certain time duration,  $t$ , at an altitude,  $h$ , from the surface, generates a pore pressure differential  $\Delta P$  within the granular media, and leads to the formation of a crater with a volume of  $V_c$ . We are able to calculate the average erosion rate,  $\dot{m}_c$  due to the various erosion processes. The other variables important for jet-induced erosion are described in Section 2.1 and shown in Eq. (B1). There are 15 dimensional parameters ( $n_{pi}$ ) which satisfy three units ( $p_{pi}$ ): length, time, and mass. Hence, 12 pi terms are needed to govern the physics.

According to previous literature and normalizing the particle mass transport rate equations (Greeley and Iversen, 1985), we believe that only a few parameters as shown in Section 2.1 need to be matched to produce dynamically similar flows. The bulk particle Reynolds number ( $Re_p$ ) for fluid flow through a packed bed is shown in Eq. (B7) with particle diameter,  $\bar{d}$ , and porosity,  $n$  is dependent on jet density,  $\rho_a$ , jet viscosity,  $\mu$  and impinging jet velocity,  $U$ . The  $Re_p$  values increase by many factors during the DGEE process due to an increase in soil porosity. The  $Kn$  is dependent on the Boltzmann constant,  $k_B$ , the ambient atmospheric pressure and temperature,  $P_{\text{amb}}$  and  $T_{\text{amb}}$ , diameter of the atmospheric molecule,  $\sigma$ , and particle size. Based on  $Kn$  at the surface atmospheric conditions of Mars and experiment, the flow dynamics are within the continuum regime. We have tabulated other dimensionless numbers such as  $Kn$ ,  $\gamma$  and nozzle area ratio for completeness (Table 4). From dimensional analysis theory, all the pi terms calculated from the experiments should be equal to the pi terms seen at full-scale to ensure complete similarity (Eq. (B18)) (Barenblatt, 2003). This is difficult to achieve for granular processes, but some pi terms have negligible effects on the physics being studied as discussed in Section 2.1.

$$V_c = f(U, D, \rho_a, g, \rho_p, \bar{d}, \mu, h, Y, n, l, t, z, c_s, \Delta P) \quad (\text{B1})$$

$$\Delta \rho = \rho_p - \rho_a \approx \rho_p \quad (\text{B2})$$

$$\Pi_1 = \frac{4V_c \rho_p n}{t \rho_a U D^2} = \frac{\dot{m}_c}{\dot{m}} \quad (\text{B3})$$

$$\Pi_2 = \frac{U}{\sqrt{g \bar{d}}} = Fr \quad (\text{B4})$$

$$\Pi_3 = \frac{\rho_a}{\rho_p} \quad (\text{B5})$$

$$\Pi_2 \sqrt{\Pi_3} = \frac{U}{\sqrt{\left(\frac{\rho_p}{\rho_a}\right) g \bar{d}}} = Fr_d \quad (\text{B6})$$

$$\Pi_4 = \frac{\rho_a U \bar{d}}{\mu(1-n)} = Re_p \quad (\text{B7})$$

$$\Pi_5 = \frac{Y}{\rho_a U^2} = \frac{Y(c, \theta_i)}{\rho_a U^2} = \beta \quad (\text{B8})$$

$$\Pi_6 = \frac{2l^2 n \mu}{k P t} = \frac{4l^2 n \mu}{k(n, d) \rho_a U^2 t} = \frac{\tau}{t} \quad (\text{B9})$$

$$\Pi_7 = \frac{h}{D} \quad (\text{B10})$$

$$\Pi_8 = \frac{l}{D} \quad (\text{B11})$$

$$\Pi_9 = \frac{\bar{d}}{D} \quad (\text{B12})$$

$$\Pi_{10} = \frac{f(\rho_a, \rho_p, \bar{d}, g)}{f(U, z, \bar{d})} = \frac{u_{*t}}{u_*} \quad (\text{B13})$$

$$\Delta P = P_p - P_{amb} \quad (\text{B14})$$

$$\Pi_{11} = \frac{3\Delta P}{2\rho_p g \bar{d}} = \Delta P^* \quad (\text{B15})$$

$$\Pi_{12} = \frac{U_g}{c_s} = \frac{f(\Delta P, \rho_p, g, \bar{d})}{c_s} = \text{Ma}_g \quad (\text{B16})$$

$$\frac{\dot{m}_c}{\dot{m}} = \phi \left( \frac{u_{*t}}{u_*}, Fr_d, Re_p, Ma_g, \frac{\tau}{\bar{t}}, \beta, n, \frac{h}{\bar{D}}, \frac{l}{\bar{D}}, \frac{\bar{d}}{\bar{D}}, \Delta P^* \right) \quad (\text{B17})$$

$$\phi(\Pi_1, \Pi_2, \Pi_3, \dots, \Pi_{n_{PI}-k_{PI}})_{\text{exp}} = \phi(\Pi_1, \Pi_2, \Pi_3, \dots, \Pi_{n_{PI}-k_{PI}})_{\text{js}} \quad (\text{B18})$$

$$Kn = \frac{k_B T_{amb}}{\sqrt{2}\pi\sigma^2 P_{amb} \bar{d}} \quad (\text{B19})$$

### Appendix C. Calculations of radial distance of dust lifting by VSE and crater volume ratio

Conservation of mass of the rocket exhaust plume is applied in determining the radial distance at which VSE dominates (Eqs. (C1) and (C2)). We assume that the compressibility effects of the impinging plume is negligible at large radial distances ( $r$ ) from the centerline (e.g., outside the crater). Assuming steady state, the freestream velocity ( $u_\infty$ ) at the centerline height ( $z$ ) of the exhaust plumes (Eqs. (C2) and (C4)) needs to be larger than the threshold freestream velocity ( $U_{\infty t}$ ) to move sand grains (Greeley and Iversen, 1985). The jet mass flow rate from all 12 nozzles,  $\dot{m}$ , at the impingement region were approximated from the nozzle exit conditions. The threshold freestream velocity is dependent on  $u_{*t}$  (Eq. (6)), the aerodynamic roughness length ( $z_0$ ) and the von Karman constant ( $\kappa$ ) as described by Eq. (C3). The aerodynamic roughness length is the height above the surface at which the flow velocity is zero and an increase in this length scale increases the value of shear stress required to initiate grain movement. The roughness length is dependent on the sand grain size.

$$\frac{\partial \rho_a}{\partial t} + \nabla \cdot (\rho_a u) = 0 \quad (\text{C1})$$

$$\dot{m} = \rho_a u A = \rho_a u_\infty \pi r^2 = \text{constant} \quad (\text{C2})$$

$$z_0 \approx \frac{2\bar{d}}{30}; \quad U_{\infty t} = \frac{1}{\kappa} u_{*t} \ln \left( \frac{z}{z_0} \right) \quad (\text{C3})$$

$$u_\infty(z) > U_{\infty t} \quad \text{Lifting of sand grains} \quad (\text{C4})$$

The volume fraction of the landing site within the Phoenix workspace that was eroded is calculated and defined as the crater volume ratio. This is the ratio of the crater volume calculated from Appendix A,  $V_c$ , to a reference soil volume,  $V_{ref}$ , which is the amount of undisturbed regolith (prior to landing) that extends to a radius of  $40D$  from the spacecraft centerline (Eq. (C5)). This is approximately the Phoenix work space area. The total crater volume for the experiments is calculated (Eq. (10)) from the erosion caused by a pair of Phoenix subscale thrusters and multiplied by six to represent all the REMs as depicted in Fig. 3A. The average crater volume ratio is obtained from experiments with soil depths of 5 cm and 20 cm with each type of simulant at Mars atmospheric pressure (Tests 1, 2, 9, 20, 21–24). These ratios derived from the experiments are compared to the crater volume ratio calculated at the Phoenix landing site (Appendix A). We approximate the Phoenix landing site by a flat surface with soil of uniform depth over an impermeable layer (subsurface ice).

$$\text{Crater volume ratio} = \frac{V_c}{V_{ref}} = \frac{V_c}{\pi(40D)^2 l} \quad (\text{C5})$$

**Table D.1**  
Normalized crater dimensions.

Test	Crater depth (a.u.)	Crater radius <sup>a</sup> (a.u.)	Exposed radius (a.u.)
1	6.4	17.6	13.6
2	1.6	19.5	13.8
3	1.6	19.8	13.7
4	7.5	28.8	10.3
5	7.4	24.6	11.4
6	7.7	24.3	10.7
7	5.1	25.9	–
8	5.9	24.3	–
9	6.0	25.6	–
10	4.8	24.3	–
11	1.6	27.3	2.6
12	2.1	4.8	–
13	0.2	4.8	–
14	2.6	4.8	–
15	1.1	6.1	–
16	2.2	3.0	–
17	1.0	7.2	–
18	1.3	8.0	–
19	2.0	8.4	–
20	2.0	8.0	–
21	1.6	35.2	20.0
22	6.4	35.8	18.1
23	1.1	4.0	–
24	1.3	3.6	–

<sup>a</sup> Crater volume calculation. Tests 1–11, 21 and 22:  $1/6 \times V_c$  from Eq. (11). Tests 12–20, 23 and 24:  $1 \times V_c$ .

### Appendix D. Normalized crater dimensions from site-alteration experiments at NASA Ames – PAL

See Table D.1.

### Appendix E. Calculations of granular temperature and speed of sound from high-speed imaging

To determine whether our flow of interest is within the subsonic, transonic or supersonic regime, the temperature and the sound speed of the granular system is calculated from high-speed imaging. Granular temperature is defined as the collision velocity fluctuations of granular particles within the system and they continually dissipate energy due to its inelasticity. However, granular flows may be excited or perturbed to increase or maintain this temperature. The granular temperature of the fluidized regions prior to granular shock formation is calculated from Eq. (E1) (Huang et al., 2006). These calculations were done for Tests 4 and 9. The granular temperature,  $T_g$ , is defined as the following:

$$T_g = \sum_{n=1}^N \frac{1}{2} |v_n(i,j) - v_b(i,j)|^2 / N \quad (\text{E1})$$

The  $v_n$  and  $v_b$  are the velocity vectors of the  $n$  particle and background velocity, respectively.  $N$  is the number of particles. These parameters were calculated using the high-speed imaging of 2-D high resolution images and a simple particle tracking software. Each image was analyzed every 2 ms. Each pixel which is  $\sim 400 \mu\text{m}$  in size in the  $x$ - $z$  plane (Fig. 4B) was tracked in both space and time. This was recorded for multiple particles along the fluidized domain during the thrust shut-down phase. Background velocity is defined as the following (Huang et al., 2006):

$$v_b(i,j) = \sum_{n=1}^N v_n(i,j) / N \quad (\text{E2})$$

The granular temperature increased during each thrust cycle, and the average value during four thrust cycles is  $\sim 0.016 \text{ m}^2/\text{s}^2$ . This trend is consistent with previous studies of high granular flow

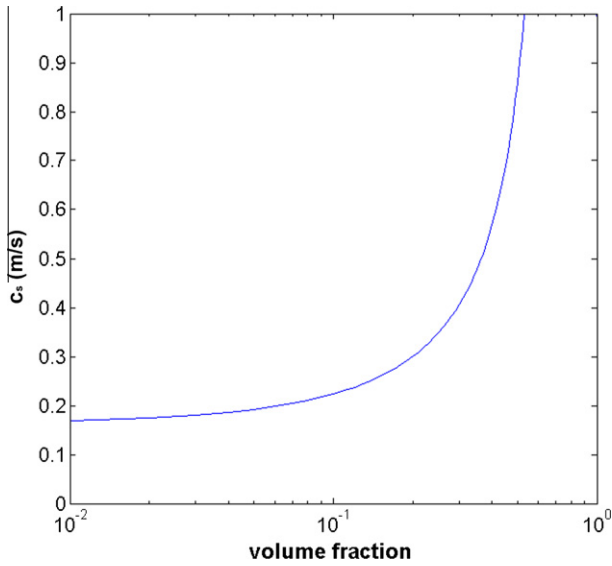


**Fig. E.1.** Speed of sound in the granular media ( $c_s$ ) vs. soil volume fraction for laboratory simulations with fine sand simulant composed of crushed walnut shells.

such as those reported by Amarouchene and Kellay (2006) and Huang et al. (2006). The speed of sound ( $c_s$ ) in the granular medium is calculated from continuum-kinetic theory (Eqs. (E3)–(E5)) where  $v$ ,  $v_m$  and  $\varepsilon$  are the soil volume fraction, maximum packing soil volume fraction and the particles coefficient of restitution (Bougie et al., 2002), and this approach shows good qualitative agreement with experimental results in Fig. S9, Section 5 of Supplementary material (Amarouchene and Kellay, 2006). As can be seen in Fig. E.1, the granular sound speed for S-type simulant is a non-linear function of porosity, volume fraction.

$$c_s = \sqrt{\frac{\partial p}{\partial \rho}} = \sqrt{T_g \chi \left[ 1 + \frac{2}{3} \chi + \left( \frac{v}{\chi} \right) \frac{\partial \chi}{\partial v} \right]} \quad (\text{E3})$$

$$\chi = 2(1 + \varepsilon)vg(v) \quad (\text{E4})$$

$$g(v) = \left[ 1 - \left( \frac{v}{v_m} \right)^{\frac{4v_m}{3}} \right]^{-1} \quad (\text{E5})$$

Analytical calculations based on continuum-kinetic theory indicates that the sound speed within the fluidized bed is approximately 0.3 m/s at a soil volume fraction of 0.2 (Fig. E.1). This is well below the speed of sound in gas and can readily support supersonic granular flow. The decrease in sound speed is predominantly due to soil particle inelastic collisions which significantly reduces the granular temperature. These calculations were used to determine the Mach number and granular flow regime. Experiments supported by Particle Image Velocimetry (PIV) are needed to directly measure the particle velocities, obtain the granular temperature and test our calculations and data interpretation.

#### Appendix F. Calculations of soil volume fraction from photometric analysis

According to Valverde et al. (2003), reflectance vs. soil volume fraction profile has been used to determine the soil volume fraction during the fluidized regime. Other researchers described in this paper have also used these photometric techniques to determine soil volume fraction ( $f_s$ ) or soil density. The intensity of the backscatter of light ( $I$ ) is recorded for various soil volume fractions as depicted in Fig. F.1. The more closely the particles are packed together (higher soil volume fraction), the higher the number of photons reflected (Hapke, 2008), causing an increase in the areal energy

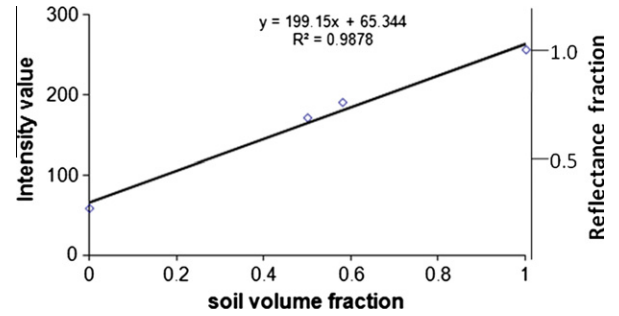


**Fig. F.1.** Reflectance vs. soil volume fraction for laboratory simulations with fine sand simulant composed of crushed walnut shells (Tests 4–20).

density of light recorded by the CMOS sensor of the camera that uses a linear gamma function. This correlates to a higher reflectance (the ratio of reflected to incident light energy) since the incident light energy on the test section is constant for all experiments.

According to Fig. F.1, the experiments show a linear correlation between reflectance and soil volume fraction with a correlation coefficient of 0.98. This is in good agreement with experiments performed by Valverde et al. (2003). The reflectance intensity (RI) is calibrated from high resolution monochromatic images at three different stages: zero soil volume fraction (58 RI = no sand grains), 1.0 soil volume fraction (256 RI = a wooden object with close to unity in porosity) and the nominal soil volume fractions (pre-jet impact) for various granular media. The high RI observed for the 1.0 soil volume fraction case may partially be attributed to specular reflectance (Hapke, 2008). In a separate experiment with similar optical setup, the fine sand is compressed and its porosity (soil volume fraction) and reflectance intensity are recorded. Four data points are available to determine the reflectance vs. soil volume fraction relationship (or calibration curve). All experiments were illuminated by 1500 W ( $\sim 10^4$  lux) of light (Fig. 4C).

More data points can be used to improve the fidelity of this calibration curve, but these results along with other published articles support a linear trend. According to Hapke (2008), this relationship is only valid for soils with an albedo smaller than  $\sim 0.9$ . The empirical equation (Eq. (F1)) derived from this curve for crushed walnut shells sized to fine sand determines the soil volume fraction from the reflectance intensity of high speed and high resolution monochromatic images. Larger uncertainty in  $f_s$  may exist at  $I$  greater than  $\sim 200$  RI.

$$f_s = \frac{I - 65.344}{199.15} \quad (\text{F1})$$

#### Appendix G. Supplementary material

Supplementary data associated with this article can be found, in the online version, at [doi:10.1016/j.icarus.2010.10.003](https://doi.org/10.1016/j.icarus.2010.10.003).

#### References

- Arvidson, R.E. et al., 2009. Results from the Mars Phoenix Lander Robotic Arm experiment. *J. Geophys. Res.* 114 (E00E02), 21.
- Amarouchene, Y., Boudet, J.F., Kellay, H., 2001. Dynamic sand dunes. *Phys. Rev. Lett.* 86, 4286–4289.
- Amarouchene, Y., Kellay, H., 2006. Speed of sound from shock fronts in granular flows. *Phys. Fluids* 18 (3), 031707-1–031707-4.
- Balme, M., Hagermann, A., 2006. Particle lifting at the soil–air interface by atmospheric pressure excursions in dust devils. *Geophys. Res. Lett.* 33 (L19S01), 5.
- Barenblatt, G.I., 2003. *Scaling*. Cambridge University Press, Cambridge, England.
- Bird, R.B., 1996. *Transport Phenomena*. John Wiley & Sons, Madison, WI.
- Bougie, J., Moon, S.J., Swift, J.B., Swinney, H.L., 2002. Shocks in vertically oscillated granular layers. *Phys. Rev. E* 66 (051301), 051301-1–051301-9.

- Buckingham, E., 1914. On physically similar systems: Illustration of the use of dimensional equations. *Phys. Rev.* 4, 345–376.
- Caesar-Ton That, T.C., Busscher, W.J., Novak, J.M., Gaskin, J.F., Kim, Y., 2008. Effects of polyacramide and organic matter on microbes associated to soil aggregation of Norfolk loamy sand. *Appl. Soil Ecol.* 40, 240–249.
- Carrier III, W.D., 2003. Particle size distribution of lunar soil. *J. Geotech. Geoenviron. Eng.* 129, 956–959.
- Christensen, E.M. et al., 1967. Surveyor V: Lunar surface mechanical properties. *Science* 158 (6301), 637–640.
- Clark, L.V., 1970. Effect of retrorocket cant angle on ground erosion – A scaled Viking study. NASA Technical Memorandum, NASA TM X-2075, Prepared by NASA Langley Research Center, Hampton, VA.
- Costa, A., 2006. Permeability–porosity relationship: A reexamination of the Kozeny–Carman equation based on a fractal pore-space geometry assumption. *Geophys. Res. Lett.* 33 (L02318), 5.
- Desai, P.N., Prince, J.L., Queen, E.M., Cruz, J.R., 2008. Entry, descent and landing performance of the Mars Phoenix Lander. In: *AIAA/AAS Astrodyn. Conf., AIAA 2008-7346*, Honolulu, Hawaii, pp. 1–13.
- Goetz, W. et al., 2009. Microscopy analysis of soils at the Phoenix landing site, Mars: Classification of soil particles and description of their optical and magnetic properties. *J. Geophys. Res.* 115 (E00E22), 23.
- Greeley, R., Iversen, J.D., 1985. *Wind as a Geological Process on Earth, Mars, Venus and Titan*. Cambridge University Press, Cambridge, England.
- Greeley, R., Leach, R., White, B., Iversen, J., Pollack, J., 1980. Threshold windspeeds for sand on Mars: Wind tunnel simulations. *Geophys. Res. Lett.* 7 (2), 121–124.
- Greeley, R., Wilson, G., Coquilla, R., White, B., Haberle, R., 2000. Windblown dust on Mars: Laboratory simulations of flux as a function of surface roughness. *Planet. Space Sci.* 48, 1349–1355.
- Greeley, R., 2002. Saltation impact as a means for raising dust on Mars. *Planet. Space Sci.* 50, 151–155.
- Greeley, R., Iversen, J.D., Pollack, J.B., Udovich, N., White, B., 1974. Wind tunnel simulations of light and dark streaks on Mars. *Science* 183 (4127), 847–849.
- Greeley, R., Leach, R.N., Williams, S.H., White, B.R., Pollack, J.B., Krinsely, D.H., Marshall, J.R., 1982. Rate of wind abrasion on Mars. *J. Geophys. Res.* 87 (B12), 10009–10024.
- Hapke, B., 2008. Bidirectional reflectance spectroscopy. 6. Effects of porosity. *Icarus* 195, 918–926.
- Hanna, J.C., Phillips, R.J., 2005. Hydrological modeling of the martian crust with applications to the pressurization of aquifers. *J. Geophys. Res.* 100 (12E01004), 19.
- Holsapple, K.A., 1993. The scaling of impact processes in planetary sciences. *Annu. Rev. Earth Planet. Sci.* 21, 333–373.
- Huang, K., Miao, G., Zhang, P., Yun, Y., Wei, R., 2006. Shock wave propagation in vibrofluidized granular materials. *Phys. Rev. E* 73, 041302-1–041302-5.
- Huseman, P.G., Bomba, J., 2000. CFD analysis of terminal descent plume impingement for Mars landers. In: *34th AIAA Thermophysics Conf. AIAA 2000-2501*, Denver, CO, pp. 1–13.
- Hutton, R.E., Moore II, H.J., Scott, R.F., Shorthill, R.W., Spitzer, C.R., 1980. Surface erosion caused on Mars from Viking descent engine plume. *Earth Moon Planets* 23 (3), 293–305.
- Jaffe, L.D., 1971. Blowing of lunar soil by Apollo 12: Surveyor 3 evidence. *Science* 171 (3973), 798–799.
- Kok, J.F., Renno, N.O., 2010. A comprehensive numerical model of steady state saltation (COMSALT). *J. Geophys. Res.* 114 (D17204), 20.
- Lee, C., Schwab, D.J., Beletsky, D., Stroud, J., Lesht, B., 2007. Numerical modeling of mixed sediment resuspension, transport, and deposition during March 1998 episodic events in southern Lake Michigan. *J. Geophys. Res.* 112, 17.
- Liu, C., Nagel, S.R., 1992. Sound in sand. *Phys. Rev. Lett.* 68 (15), 2301–2304.
- Markiewicz, W.J. et al., 2009. Sublimation of exposed Snow Queen surface water ice as observed by the Phoenix Mars Lander. *Lunar Planet. Sci.* 40. NASA Johnson Space Center.
- Mazurek, K.A., Rajaratnam, N., 2005. Erosion of sand beds by obliquely impinging plane turbulent air jets. *J. Hyd. Res.* 43 (5), 567–573.
- Mason, C.C., 1970. Comparison of actual vs. predicted lunar surface erosion caused by Apollo 11 descent engine. *Geol. Soc. Am. Bull.* 81 (6), 1807–1812.
- Mellon, M.T. et al., 2009. Ground ice at the Phoenix landing site: Stability state and origin. *J. Geophys. Res. – Planets* 114 (E00E07), 13.
- Mehta, M., Renno, N.O., Cotel, A.J., Grover, M.R., 2007. Characterization of the impingement dynamics of pulsed rocket plumes with the ground at low ambient pressure. In: *43rd AIAA/ASME/ASCE/SAE Joint Prop. Conf., AIAA 2007-5707*, Cincinnati, OH, pp. 1–11.
- Mehta, M., Renno, N.O., Grover, M.R., Marshall, J., Woosley, C., Rusche, N., 2008. Site alteration and dust lifting during simulated Phoenix Mars landing. NASA JPL Internal Memorandum, Prepared by U. of Michigan Dept. of Atmos., Oceanic & Space Sciences for NASA JPL, Pasadena, CA.
- Metzger, P.T., Immer, C.D., Donahue, C.M., Vu, B.T., Latta, R.C., Deyo-Svendsen, M., 2009a. Jet-induced cratering of a granular surface with applications to lunar spaceports. *J. Aerosp. Eng.* 22 (1), 24–32.
- Metzger, P.T., Lane, J.E., Immer, C.D., Clements, S., 2009b. Cratering and blowing soil by rocket engines during lunar landings. In: *Beneraoya, H. (Ed.), Lunar Settlements*. CRC Press, pp. 551–578.
- Neakrase, L.D.V., Greeley, R., 2009. Dust devil sediment flux on Earth and Mars: Laboratory simulations. *Icarus* 206 (1), 306–318.
- Plemmons, D.H., Mehta, M., Clark, B.C., Kounaves, S.P., Peach, L.L., Renno, N.O., Tamparri, L., Young, S.M.M., 2008. Effects of the Phoenix lander descent thruster plume on the martian surface. *J. Geophys. Res.* 113 (E00A11), 16.
- Pudasaini, S.P., Kroner, C., 2008. Shock waves in rapid flows of dense granular materials: Theoretical predictions and experimental results. *Phys. Rev. E* 041308, 11.
- Renno, N.O. et al., 2009. Possible physical and thermodynamical evidence of liquid water at the Phoenix landing site. *J. Geophys. Res.* 114 (E00E03), 11.
- Romine, G.L., Reiser, T.D., Gliozzi, J., 1973. Site alteration effects from thruster exhaust impingement during a simulated Viking Mars landing: Nozzle development and physical site alteration. NASA Contractor Report, NASA CR-2252, Prepared by Martin Marietta Aerospace, Denver, CO, for NASA Langley Research Center, Washington, DC.
- Schlichting, H., Gersten, K., 2000. *Boundary Layer Theory*. Springer-Verlag Publishing, New York.
- Schultz, P.H., Eberhardy, C.A., Ernst, C.M., A'Hearn, M.F., Sunshine, J.M., Lisse, C., 2007. The Deep Impact oblique impact cratering experiment. *Icarus* 190 (2), 295–333.
- Scott, R.F., Ko, H.-Y., 1968. Transient rocket-engine gas flow in soil. *AIAA J.* 6 (2), 258–264.
- Shao, Y., Lu, H., 2000. A simple expression for wind erosion threshold friction velocity. *J. Geophys. Res.* 105 (D17), 22437–22444.
- Shaw, A., Arvidson, R.E., Bonitz, R., Carsten, J., Keller, H.U., Lemmon, M.T., Robinson, M., Trebi-Ollennu, A., 2009. Phoenix soil physical properties investigation. *J. Geophys. Res.* 114 (E00E05), 19.
- Shorthill, R.W., Hutton, R.E., Moore II, H.J., Scott, R.F., Spitzer, C.R., 1976a. Physical properties of the martian soil surface from Viking 1 Lander: Preliminary results. *Science* 193, 805–809.
- Shorthill, R.W., Moore II, H.J., Hutton, R.E., Scott, R.F., Spitzer, C.R., 1976b. The environment of Viking 2 Lander. *Science* 194, 1309–1318.
- Sizemore, H.G., Mellon, M.T., Searls, M.L., Lemmon, M.T., Zent, A.P., Heet, T.L., Arvidson, R.E., Blaney, D.L., Keller, H.U., and the Phoenix Science Team, 2009. In situ analysis of ice table depth variations in the vicinity of small rocks at the Phoenix landing site. *J. Geophys. Res.* 115 (E00E09), 12.
- Sizemore, H.G., Mellon, M., 2008. Laboratory characterization of the structural properties controlling dynamical gas transport in Mars-analog soils. *Icarus* 197 (2), 606–620.
- Smith, P.H. et al., 2009. H<sub>2</sub>O at the Phoenix landing site. *Science* 325 (5936), 58–61.
- Teruel, F.E., Rizwaan-uddin, 2009. A new turbulence model for porous media flows. Part II: Analysis and validation using microscopic simulations. *Int. J. Heat Mass Transf.* 52, 5193–5203.
- Terzaghi, K., 1943. *Theoretical Soil Mechanics*. John Wiley and Sons, New York.
- Townsend, A.A., 1956. *The Structure of Turbulent Shear Flow*. Cambridge Univ. Press, London, England.
- Valverde, J.M., Quintanilla, M.A.S., Castellanos, A., Mills, P., 2003. Experimental study on the dynamics of gas-fluidized beds. *Phys. Rev. E* 67 (016303), 016303-1–016303-5.
- Van Norman, J.W., Novak, L., 2009. CFD support of MSL MLE plume simulations. NASA Contractor Report, Contract No. NNL04AA03Z, Prepared by AMA Inc. for NASA, Washington, DC.